High-pressure behavior and crystal-fluid interaction in natural erionite-K

Tommaso Battiston[a,*], Davide Comboni[b], Francesco Pagliaro[a],

Paolo Lotti[a], Michael Hanfland[b], G. Diego Gatta[a]

[a]Dipartimento di Scienze della Terra, Università degli Studi di Milano, Via Botticelli 23, 20133 Milano, Italy

[b]European Synchrotron Radiation Facility, 71 Avenue des Martyrs, CS40220, 38043 Grenoble Cedex, France

* Corresponding author.
Email adress: tommaso.battiston@unimi.it (T. Battiston)

Abstract:

The high-pressure behavior of a natural erionite-K has been investigated by in situ single-crystal synchrotron X-ray diffraction with a diamond anvil cell (DAC), using four different P-transmitting fluids: the non-penetrating silicone oil and the potentially penetrating methanol:ethanol:H_2O = 16:3:1 mixture, pure H_2O and naturally hydrated glycerol. The investigated crystals showed typical offretite stacking faults in the diffraction pattern. The experiment in silicone oil showed that the erionite bulk compressibility lies within the range observed for the previously investigated zeolites, as its refined bulk modulus ($K_{V0} = 1/\beta_{V0}$), calculated within the range P_{amb}-1.52(5) GPa, resulted equal to 47(2) GPa. The high-pressure experiments performed using potentially penetrating P-transmitting fluids showed significantly lower compressibilities, unambiguously suggesting the P-mediated intrusion of new molecules into the structural voids. Further evidence is provided by the comparative analysis of the framework deformation mechanisms: erionite-K compressed in *m.e.w.* showed a drastically lower compressibility of the erionite cage, with respect to silicone oil. In conclusion, this study suggests natural erionite, a relatively common zeolite, as a suitable candidate for the P-mediated intrusion and hyper-confinement of molecules into the framework microcavities.

1) Introduction:

Natural zeolites can be considered a class of strategic minerals for many technical applications [1,2,3]. During the last decades, several studies have focused on the high-pressure behavior of natural and synthetic zeolites hydrostatically compressed in different P-transmitting fluids (PTFs) [4,5], also to determine the potential exploitability of the high-pressure (HP) phenomena. Hydrostatic pressure, at a kilobar level, was proven to govern a series of interesting phenomena in zeolites, based on the crystal-fluid interactions. This led to distinguish between the so-called potentially "penetrating" P-transmitting fluids (PTFs), *i.e.,* those with a kinetic diameter of atoms or molecules sufficiently small to intrude the zeolites' structural voids, and the counter-part represented by potentially "non-penetrating" fluids, *i.e.,* those that cannot penetrate the cavities. While "non-penetrating" PTFs allow to investigate the intrinsic compressibility, P-induced phase transitions and amorphization processes of a given zeolite, the penetrating ones can be adopted to explore the labyrinthine world of the P-induced crystal-fluid interactions [6,7,4, for a review]. These phenomena can be exploited to improve catalytic performances of microporous materials [8] or for tailoring new functional compounds, *e.g.* with a controlled extra-framework content or a stiffened structure [4,9], or even to describe a series of natural phenomena in which zeolites act as carrier of fluids [6,7]. However, the behavior of many zeolites has not been already investigated at high pressure.

In this manuscript, we report the high-pressure behavior of a natural erionite, studied by means of *in-situ* HP single-crystal synchrotron X-ray diffraction, and, to the best of our knowledge, the first occurrence of P-induced intrusion of molecules into the structural cavities of this zeolite. Erionite, with general chemical formula $(K_2Na_2Ca_3)[Al_{10}Si_{26}O_{72}]\cdot30H_2O$ [10], is usually characterized by woolly/fibrous morphology and has been described for the first time by Eakle in 1898 [11]. In nature, it shows a wide chemical variability [10,12,13], expressed as a solid solution among three end-

members: erionite-Ca, erionite-K and erionite-Na, according to the most abundant extraframework cation [12]. Erionite crystallizes in the hexagonal system, with space group $P6_3/mmc$. Its crystal structure was first described by Staples and Gard in 1959 [14], and subsequently confirmed by further studies [15]. The erionite framework [ERI] is characterized by the presence of large cages (23-hedron, called "erionite-cage"), with a maximum free diameter of ~ 8.1 Å, bounded along the c-axis by six-membered rings of $(Si,Al)O_4$ tetrahedra (hereafter 6mR) (~ 3.8 Å free diameter) (Fig. 1a-b). Large eight-membered rings of tetrahedra (hereafter 8mRs) laterally mark the boundaries of the cages (Fig. 1b). Channels, made by alternating cancrinite-cages and double six rings (D6R), run parallel to the erionite-cages (Fig. 1a). According to the classification given by Gottardi and Galli [16], slightly modified by Armbruster and Gunter [17], erionite belongs to the "group of zeolites with six-membered rings". In terms of repetition of 6mRs, the ERI framework can be generated with a stacking sequence of AABAAC rings. For their similar framework structures, intergrowths of erionite and offretite have been often reported [10,12,15,18], being the offretite framework [OFF] given by the repetition of a 6mR with an AAB sequence. Consequently, stacking faults involving the B and C positions commonly lead to the alternation of the [ERI] and [OFF] frameworks along the c crystallographic direction, making very common the intergrowth of the two structures.

Erionite, along with other fibrous aluminosilicate minerals, *e.g.*, asbestos minerals, is classified in "Group 1 – Carcinogenic to humans" by the International Agency for Research on Cancer, due to the high incidence of pleural and peritoneal mesothelioma that can be causally associated with its exposure [19]. Erionite has been the first and only natural zeolite commercially used in the refinery industry in the *Selectoforming* catalytic process (in 1968) [20,21]. Recently, several investigations were aimed to constrain ion-exchange and catalytic properties of this zeolite [22–24].
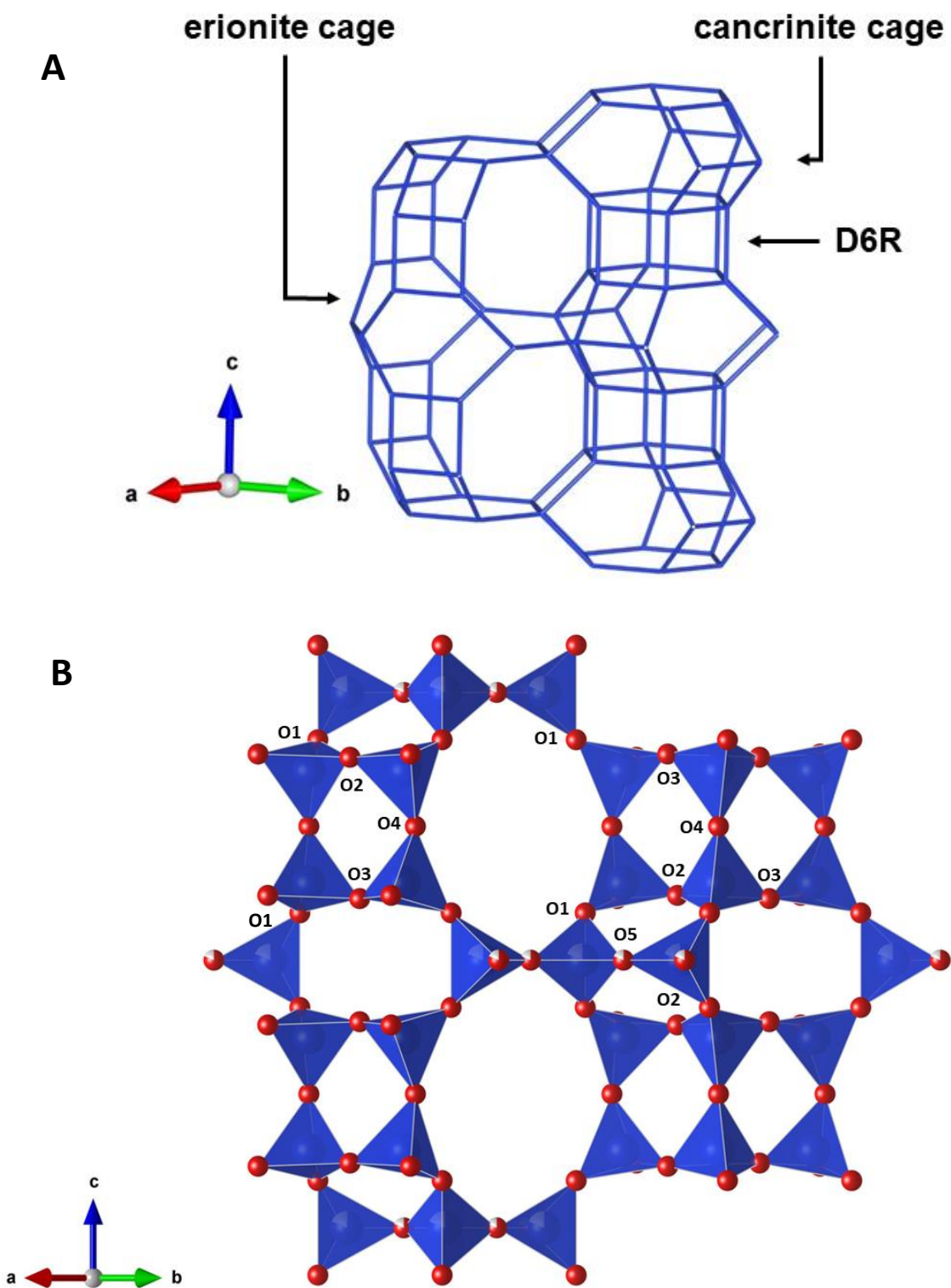
Fig. 1: View of the ERI-framework type, with the erionite-cage on the left and the repetition of cancrinite-cage/D6R on the right: (A) Skeletal view; (B) tetrahedral view

73   The behavior at non-ambient conditions of erionite has been investigated at varying temperature

74 [25–27], whereas, to the best of our knowledge, no data on the compressional behavior nor on the *P*-

75 induced zeolite-fluid interactions are available. This high-pressure study on erionite represents a

76 further step in the framework of a long-term project devoted to investigating the crystal-fluid

77 interaction in microporous compounds [8,28–31].

78 **2) Materials and experimental methods:**

79 *2.1) Samples selection and chemical analysis*

80 Natural erionite single crystals from Chase Creek, Falkland, British Columbia, Canada, were

81 selected for our investigations. Preliminary identification was performed by single-crystal X-ray

82 diffraction, using a Xcalibur Oxford-Diffraction diffractometer (equipped with a CCD detector,

83 graphite-monochromatized Mo-*K*α radiation, and operating at 50 kV and 30 mA), at the Earth

84 Sciences Department of the University of Milan (ESD-MI). The crystals, prismatic and similar in size

85 (~$250 \times 60 \times 60$ μm^3), were all free of twinning. On the same crystals, chemical microanalysis was

86 performed by electron microprobe in wavelength dispersive mode (EMPA-WDS), using a JEOL

87 JXA-8200 instrument at the ESD-MI. Data were collected operating with an accelerating voltage of

88 15 KeV, a beam current of 5 nA, a defocused beam width of 20 μm and counting time of 30 and 10 s

89 for the peaks and the background, respectively. Correction for the matrix effect on raw data was

90 applied using the *PhiRhoZ* method, implemented in the JEOL suite of programs. Natural samples

91 were used as standards (Ca, Al, Si – grossular; K – K-feldspar; Na – omphacite; Mg – forsterite; Sr –

92 celestine; Ba – sanbornite). The investigated crystals were chemically homogeneous; only slight

93 variations in the Mg content were observed. The chemical formula, averaged from 20 point analyses

94 and calculated on the basis of 72 O a.p.f.u., is:

95 $(K_{2.39}Na_{0.11}Ca_{1.99}Mg_{1.02}Sr_{0.03}Ba_{0.04})[Al_{9.02}Si_{27.05}]O_{72} \cdot 26.84(H_2O)$. According to the most abundant

96 extra-framework cation, the erionite sample can be classified as erionite-K.

97 For a full structural characterization, a single crystal, ~ $100 \times 35 \times 35$ μm^3 in size, was selected for a

98 X-ray diffraction data collection in air, performed at the ESD-MI with a Rigaku XtaLAB Synergy-S

diffractometer equipped with a HyPix-6000HE detector and a PhotonJet-S Mo-$K\alpha$ (λ=0.71073 Å)
microsource, operating at 50 kV and 1 mA. X-ray diffraction data were collected with an omega step
size of 0.5° and 40 s per step of exposure time. Indexing of the diffraction pattern, unit-cell parameters
refinement and intensity integration were performed using the *CrysAlisPro* software [32].

2.2) *High-pressure experiments*

Single-crystal X-ray diffraction experiments at *in-situ* high-P conditions were performed at the
ID15B beamline of the European Synchrotron Radiation Facility (ESRF) in Grenoble, France.
Transparent crystals with a prismatic habit ($\sim 60 \times 30 \times 30 \ \mu m^3$ in size) were selected for the high-
pressure experiments. Crystals with a comparable fraction of offretite intergrowth (see section 3 for
further details) were selected, to avoid any bias (due to of the offretite content) on the P-induced
crystal-fluid interactions. High-pressure conditions were generated by means of a membrane-driven
diamond anvil cell (DAC), mounting Boehler-Almax designed diamonds (culet diameter 600 μm).
For each high-pressure ramp, erionite crystals were loaded into the P-chamber along with few ruby
chips as P-calibrant (by the ruby fluorescence method, P-uncertainties ~0.05 GPa [33,34]). For each
experiment, the P-chamber was obtained using a stainless-steel gasket pre-indented to 70 μm and
drilled by spark erosion (hole diameter ~ 200 μm). *In situ* HP-experiments were performed using four
different P-transmitting fluids: 1) silicone oil (s.o.), up to 1.52(5) GPa, slightly higher than its
hydrostatic limit [35]; 2) 16:3:1 methanol:ethanol:H_2O mixture (m.e.w., kinetic diameters: H_2O ~
2.65 Å, methanol ~ 3.76 Å, ethanol ~ 4.46 Å) up to 3.49(5) GPa, below its hydrostatic limit [35]; 3)
pure H_2O up to 0.99(5) GPa, due to the transition to ice; 4) naturally-hydrated glycerol (n.h.glyc.,
kinetic diameter: glycerol ~ 6.1 Å; water content unknown) up to 4.49(5) GPa. According to the ERI
framework free diameters [36], m.e.w. and pure H_2O, can be considered as potentially penetrating P-
transmitting fluids [6], while s.o., due to its polymeric nature, is not able to penetrate the structural
cavities in response to the applied pressure. Concerning n.h.glyc, glycerol molecules are nominally
non-penetrating, but P-induced intrusion phenomena of its H_2O fraction may be observed. For all the

124 ramps, the data collection strategy always consisted in a stepwise ω-rotation in the range ± 32°, with

125 0.5° step width, and 0.2 s of exposure time per step. The experimental setup provides a parallel

126 monochromatic beam (E = 30 KeV, λ = 0.4107 Å), and the diffraction patterns were collected by an

127 *Eiger2 9M CdTe* (340x370 mm) flat-panel detector positioned at a distance of 180.68 mm from the

128 sample. Further details on the beamline experimental setup are reported in [37]. Indexing of

129 diffraction patterns, unit-cell parameters refinement and intensity integration were performed using

130 the *CrysAlisPro* software [32]. Adsorption (due to the DAC components) and background corrections

131 were applied adopting the semiempirical *ABSPACK* routine implemented in the *CrysAlisPro* suite.

132 **3) Crystal structure refinement**

133 Structure refinements, at ambient and high-P conditions, were performed using the software

134 *JANA2006* [38] in the space group $P6_3/mmc$. The structure refinement based on the data collected at

135 ambient conditions (data collected in home-lab, ESD-MI) was performed starting from the framework

136 model of Gualtieri et al. [12]. Residual peaks in the difference-Fourier maps of the electron density,

137 ascribable to the Si and O positions of the intergrown offretite framework (Fig. S1), were detected

138 and assigned to as Si2', O5' and O6', mutually exclusive with Si2, O5 and O6 pertaining to the

139 erionite framework. The Si2', O5' and O6' were constrained to share the same occupancies and

140 (isotropic) displacement parameters. The occupancies of the sites Si2 and Si2', O5 and O5', and O6

141 and O6', belonging to the erionite and offretite intergrowths, respectively, were restrained to a sum

142 of 1.0. Extraframework cations and H_2O molecules were located after a careful analysis of the

143 difference-Fourier maps of the electron density. The cancrinite-cage was found to be filled by a single

144 K site, labelled as K1, bonded to O2 and O3 in a trigonal prismatic coordination; the structure

145 refinement confirmed a full occupancy of the K site. The other extraframework ions and molecules

146 populate the erionite cage. Three Ca and one Mg sites, some of which mutually exclusive, were

147 located along the ternary axis at ⅓, ⅔, z, labelled as Ca1, Ca2, Ca3 and Mg (Fig. S2a and Tab. 1), all

148 coordinating H_2O molecules. An additional K site, labelled as K2, was located at ½, 0, 0 (Fig. S2a),

149 in the centre of the eight-membered ring (8mRs) connecting adjacent erionite cages, with a partial

150 occupancy of ~ 0.2. Five weaker residues in the difference-Fourier maps were refined as H_2O-oxygen

151 sites, labelled as Ow7, Ow8, Ow9, Ow10, and Ow11. All the H_2O-oxygen sites lie within the erionite

152 cage at different z coordinates: while Ow7, Ow8, Ow10 and Ow11 are coordinated by Ca and Mg

153 atoms, Ow9 is in the proximity of the 8mR connecting adjacent erionite cages and mutually exclusive

154 with K2. Anisotropic displacement parameters (D.P.) were refined only for the framework atomic

155 positions, while the extraframework sites were refined as isotropic, due to the effect of positional

156 disorder. The H_2O-oxygen sites were constrained to share the same D.P., which was fixed to the value

157 that provided the best figure of merit of the refinement and which takes into account the significant

158 positional disorder of the H_2O molecules (as suggested by distribution of electron density in the

159 difference-Fourier maps), *i.e.* 0.15 $Å^2$.

160 In structure refinements based on the high-P data, further restrictions were applied to reduce

161 the number of refined variables: 1) the occupancies of the mutually exclusive sites Si2 and Si2', O5

162 and O5', and O6 and O6' were refined at room conditions (with the same restrictions described above)

163 and then fixed to those values for the HP refinements; 2) the occupancies of the extraframework

164 cation sites were fixed at the values refined at ambient conditions, whereas the occupancies of the

165 H_2O-oxygen sites were always refined in order to investigate the potential P-intrusion of molecules

166 into the structural cavities. In this light, no restrictions were applied to the site occupancy factors of

167 H_2O oxygens and, to minimize any bias from the other structural variables, their D.P. parameters

168 have always been kept fixed to the value of 0.15 $Å^2$, adopted for the ambient-conditions refinement.

169 By applying this strategy, the refined values of the H_2O-oxygen sites occupancies should not be

170 interpreted as a quantitative measure of the site H_2O content, as this is influenced by the arbitrary

171 modelling of an isotropic and fixed displacement parameter. However, this allows a direct comparison

172 of the relative increase or decrease of H_2O molecules per unit-cell between different pressure points

173 within a compressional ramp and among different compressional ramps, as discussed in section 5.2.

174 In addition, in order to reduce the number of refined variables, the displacement parameters of the

175   framework sites were refined as isotropic, whereas those of the extraframework cationic sites were

176   also kept fixed to the values refined at ambient conditions. The Si2'-O bond distances were restrained

177   to 1.64 (2) Å. Atomic sites coordinates, occupancies and D.P.'s from the ambient-conditions

178   refinement are reported in Tab. 1. Selected statistical parameters of the refinements are reported in

179   Tab. S1, whereas H_2O oxygen refined occupancies from each structure refinements are reported in

180   Tab S2. Selected refined structural models (CIF files) are deposited as supplementary materials.

181

182 **Tab. 1:** Atomic fractional coordinates, site occupancy factors (*s.o.f.*) and thermal displacement parameters
183 (Å^2) at room conditions.

site	x	y	z	*s.o.f.*	U_{iso}/U_{eq}
Si1	0.23386(12)	0.99986(13)	0.10476(10)	1	0.0146(6)
Si2	0.09366(19)	0.42530(18)	1/4	0.894(4)	0.0133(9)
Si2'	0.0892(14)	0.4217(14)	3/4	0.106(4)	0.0133(9)
O1	0.3481(3)	0.0247(4)	0.6610(3)	1	0.038(2)
O2	0.0987(2)	0.01975(5)	0.01277(4)	1	0.030(2)
O3	0.1254(3)	0.2508(6)	0.6342(4)	1	0.039(3)
O4	0.2640(4	0	0	1	0.029(2)
O5	0.2319(3)	0.4638(7)	1/4	0.894(4)	0.027(4)
O5'	0.237(4)	0.474(9)	3/4	0.106(4)	0.027(4)
O6	0.4594(4)	0.9188(8)	1/4	0.894(4)	0.031(4)
O6'	0.454(3)	0.907(6)	3/4	0.106(4)	0.031(4)
K1	0	0	1/4	0.994(18)	0.0299(17)
K2	1/2	0	0.00	0.210(3)	0.15*
Mg	1/3	2/3	0.519(5)	0.18(2)	0.103(2)
Ca1	1/3	2/3	0.904(3)	0.216(14)	0.103(8)
Ca2	1/3	2/3	0.119(2)	0.224(14)	0.103(8)
Ca3	1/3	2/3	0.696(2)	0.177(12)	0.103(8)
Ow7	0.241(4)	0.482(9)	3/4`	0.54(15)	0.15*
Ow8	0.495(4)	0.7475(18)	0.507(3)	0.33(2)	0.15*
Ow9	0.446(2)	0.893(4)	0.010(3)	0.30(2)	0.15*
Ow10	0.4271(11)	0.854(2)	0.894(2)	0.50(2)	0.15*
Ow11	0.255(4)	0.510(9)	0.703(13)	0.21(8)	0.15*

* Fixed parameter, see Section 3 for further details

4) Results

4.1) HP elastic behavior

The *P*-induced evolution of the unit-cell parameters is listed in Tab. S3 and shown in Fig. 2. No phase transition has been observed in response to the applied pressure. The compressional paths of the cell parameters in m.e.w. and n.h.glyc appear to be completely reversible, as suggested by the data collected in decompression. Comparing the *P*-*V* patterns using different *P*-transmitting media clearly shows that natural erionite is more compressible in the non-penetrating silicone oil, if compared to the other media.
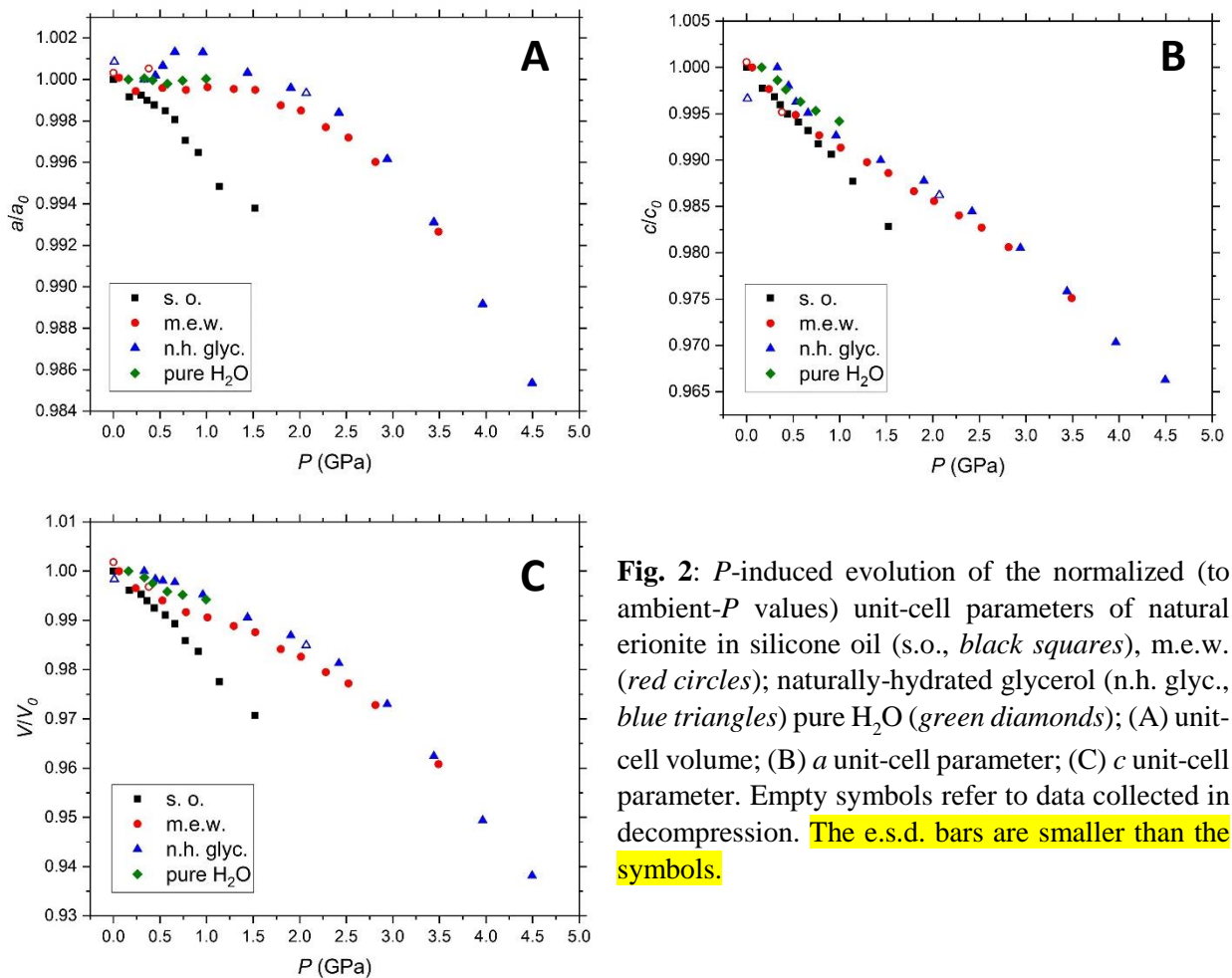
Fig. 2: *P*-induced evolution of the normalized (to ambient-*P* values) unit-cell parameters of natural erionite in silicone oil (s.o., *black squares*), m.e.w. (*red circles*); naturally-hydrated glycerol (n.h. glyc., *blue triangles*) pure H_2O (*green diamonds*); (A) unit-cell volume; (B) *a* unit-cell parameter; (C) *c* unit-cell parameter. Empty symbols refer to data collected in decompression. The e.s.d. bars are smaller than the symbols.

196   This is likely the effect of the P-induced intrusion of molecules from the penetrating fluids through

197   the cavities (Fig. 2), which fill the voids making the framework less compressible. Glycerol is

198   nominally a non-penetrating fluid [5,7], but we presume that its spontaneous hydration can also lead

199   to a H_2O molecules penetration when used as P-fluid. Figure 2 and Table S3 show that, in s.o., erionite

200   undergoes a monotonic compression up to 0.66(5) GPa, followed by a slight increase in

201   compressibility up to 1.52(5) GPa. On the contrary, in m.e.w. erionite follows the same trend only up

202   to 0.24(5) GPa, then a decrease in compressibility is observed, followed by a softening at $P>1.52(5)$

203   GPa. In n.h. glyc, the P-V data suggest an even lower compressibility in the low-P regime, followed

204   by a trend similar to that observed in m.e.w. at $P > 1$ GPa. A similar behavior to that observed in n.h.

205   glyc. is observed for the compression in pure H_2O up to 0.99(5) GPa.

206   Different anisotropic compressional behaviors can be observed when different fluids are used (Fig.

207   2b, 2c). The compressibility along the c-axis is similar for all the experiments up to 0.78(5) GPa.

208   Above that pressure, while the behavior in s.o. is almost monotonic, a decrease in compressibility in

209   n.h. glyc. and in m.e.w. can be observed. In contrast, along the a-axis (which reflects the behavior of

210   the (0001) plane), a significantly different compressional path is observed among the ramps in

211   silicone oil and in penetrating fluids. Along the a axis, the structure is substantially uncompressible

212   at $P < 1.5$ GPa in penetrating fluids, with even an expansion observed between $ca.$ 0.5 and 1.0 GPa

213   in n.h. glyc. As it will be discussed below, in the structure refinement based on the data collected at

214   0.65(5) GPa (P4) in n.h. glyc., evidences of crystal-fluid interaction were observed (Fig. 3a-d), which

215   can be invoked to explain its different compressional path with respect to the compression in other

216   fluids.
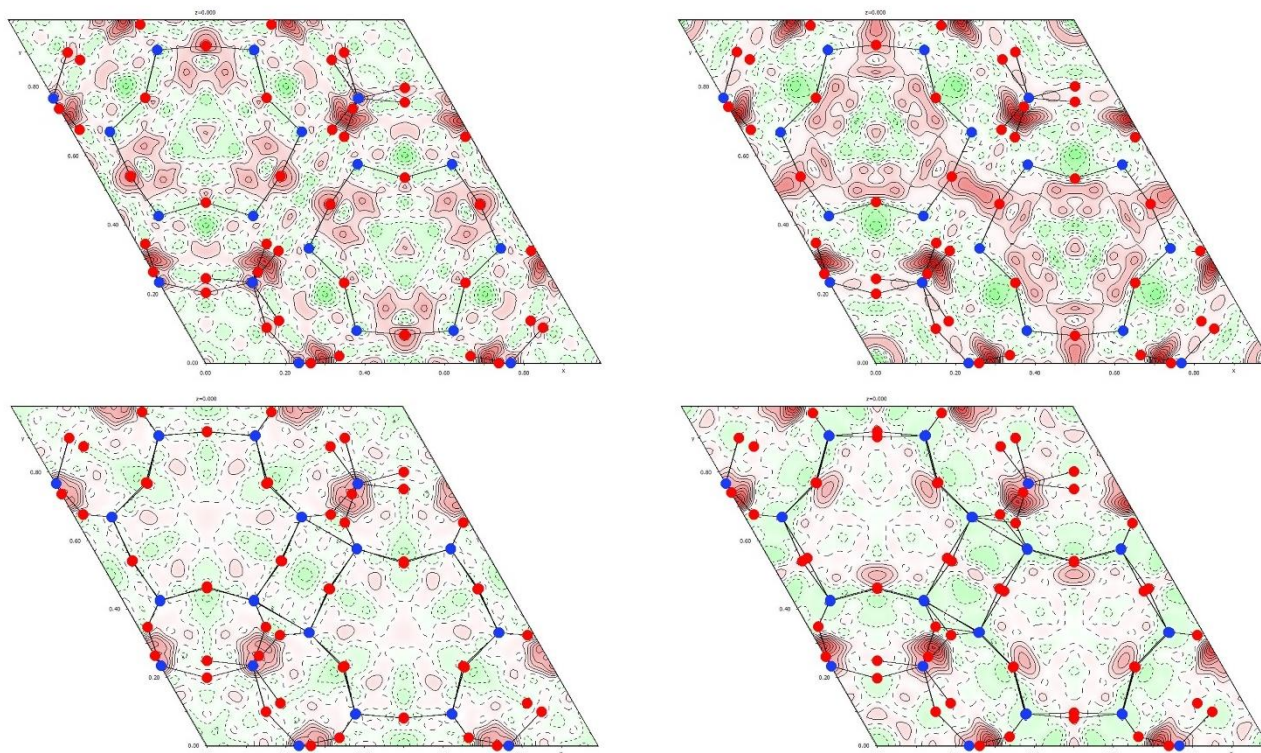
Fig. 3: Section of the unit cell at $z = 0$ ($0 \leq x \leq 1$; $0 \leq y \leq 1$) showing the residual peaks (green positive and red negative) in the difference-Fourier maps of the electron density from: (A) n.h. glyc. experiment [0.33(5) GPa]; (B) n.h. glyc. [0.66(5) GPa]; (C); m.e.w experiment [0.06(5) GPa] (D) m.e.w. experiment [0.52(5) GPa]. An elongated positive residue can be observed at the center of the 8mR connecting two adjacent erionite cages from the n.h. glyc. experiment. This residue is absent in the m.e.w. structure refinement. Red circles represent O atoms; blue circles represent Si atoms. Extraframework atoms are not reported.

218   Experimental *P-V* data collected in silicone oil (representing the intrinsic compressional behavior of

219   natural erionite), weighted by their uncertainties, have been fitted to a Birch-Murnaghan equation of

220   state (BM-EoS) truncated to the second order (II-BM EoS) in energy, using the *EoSFit 7.0 GUI*

221   software [39,40]. This isothermal EoS is based on the assumption that the strain energy of a solid

222   undergoing compression can be expressed as a Taylor series in the finite Eulerian strain, $fe = [(V_0/V)$

223    $^{2/3}-1]/2$ (where V_0 represents the volume at ambient pressure and temperature) [40]. Expansion in the

224   Eulerian strain has the following form:

225    $P(fe) = 3K_{P0,T0} fe (1+2fe)^{5/2} \{1+ 3/2 (K'-4) fe + 3/2[K_{P0,T0} K" + (K'-4) (K'-3) + 35/9] fe^2 + \dots \}$

226   where $K_{P0,T0}$ is the isothermal bulk modulus, defined as $K_{P0,T0} = -V^{-1}(\partial P/\partial V)_{T0} = \beta^{-1}{}_{P0,T0}$ ($\beta_{P0,T0}$ is the

227   volume compressibility coefficient at room conditions) and $K' = \partial K_{P0,T0}/\partial P$ and $K" = \partial^2 K_{P0,T0}/\partial P^2$.

228   The refined isothermal bulk modulus, based on the data in the range P_{amb}-1.52(5) GPa, is $K_{V0} = 47(2)$

229   GPa ($V_0 = 2298(1)$ Å^3). In order to take into account the observed change in compressibility

230   previously described, two separate fits have been also performed in the ranges P_{amb}-0.66(5) and

231   0.77(5)-1.52(5) yielding, respectively, to the following refined parameters: $V_0 = 2295(1)$ Å^3 and K_{V0}

232    $= 62(6)$ GPa, and $V_0 = 2303(5)$ Å^3 and $K_{V0} = 42(4)$ GPa. Linearized II-BM EoS [39] have been fitted

233   to the *a-P* and *c-P* data and the refined parameters are reported in Table 2.

234

Tab. 2: Refined elastic parameters of natural erionite based on II-BM equation of state fits.

s. o.	P (GPa)	V_0, l_0 (Å^3, Å)	$K_{V0,l0}$ (GPa)	K'
V	0.00-1.52(5)	2298(1)	47(2)	4
a	0.00-1.52(5)	13.270(3)	72(5)	4
c	0.00-1.52(5)	15.077(5)	27(1)	4
m.e.w.				
V	0.06(5)-2.01(5)	2291(1)	115(6)	4
V	2.01(5)-3.49(5)	2337(9)	53(5)	4
n.h. glyc				
V	0.32(5)-2.41(5)	2293.3(9)	108(4)	4
V	2.41(5)-4.38(5)	2399(13)	32(2)	4
pure H_2O				
V	0.16(5)-0.99(5)	2300(1)	129(15)	4

237   *4.2) P-induced structure deformation*

238   After a careful analysis of the residual peaks in the difference-Fourier maps of the electron density

239   function, two new H_2O-oxygen atomic sites, labelled as Ow12 and Ow13, have been included into

240   the structure model starting, respectively, from 0.53(5) and 0.78(5) GPa for the m.e.w. ramp, and

241   0.42(5) and 0.33(5) GPa for the ramp in pure H_2O. These sites correspond to sites already partially

242   occupied by the Mg and K as extraframework cations. For the n.h. glyc. experiment, only the Ow13

243   site was included into the model. No significant evidence of new extraframework sites was observed

244   for the experiment based on the s.o. ramp.

245   The evolution of the refined occupancies of H_2O-oxygen atomic sites in response to applied

246   pressure, expressed as the overall number of refined electrons, is reported in Fig. 4 and in Tab. S2. It

247   can be observed the horizontal trend in the s.o. experiment, compared to the increasing trends (up to

248   ~ 2.50 GPa) observed in m.e.w. and n.h. glyc, ascribable to the intrusion of new fluids molecules into

249   the framework cavities (see section 5.2).
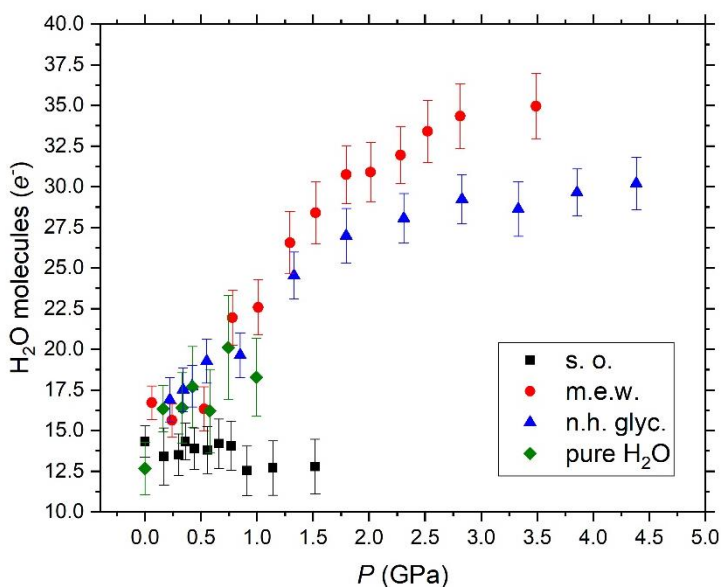

Fig. 4: *P*-induced evolution of the overall H_2O-oxygen sites occupancy, expressed as the sum of the refined electrons of all the H_2O-oxygen extraframework sites. Data from the silicone oil experiment (s.o.) in black squares, from m.e.w. in red circles, from naturally hydrated glycerol (n.h. glyc.) in blue triangles and from the pure H_2O experiment in green diamonds.

250

To better describe the *P*-induced structural deformation and crystal-fluid interaction in erionite, the volume of the ERI-cage has been modelled according to the protocol described in the Appendix 1. The high-pressure evolution of the so-modelled erionite-cage volume is reported in Tab. S4 and Fig. 5a. An abrupt decrease in compressibility, starting around 0.50(5) GPa up to 1.50(5)-2.00(5) GPa, is observed for the m.e.w. experimental data.

An analysis of the evolution of the structural parameters in response to the applied pressure was performed only for m.e.w. and s.o. structure refinements, due to their better data quality. The results, reported in Tab. S4, Tab. S5, Fig. 5 and Fig. S3, show which are the main structural deformation mechanisms of the framework, at the atomic scale, involving the cancrinite-cage and D6R channel: *i.e.*, the evolution of O2-O5-O2 and O2-O4-O3 interatomic angles (Fig. 1b). An increase of the di-trigonal distortion of the 6mR in cancrinite-cage, shown by the evolution of O3-O2-O3 angle (Fig. 5c, S2b and Tab. S4), was observed up to ~ 1 GPa in both experiments. Above this pressure, a partial recovery of the original shape of the ring was observed from the m.e.w data. The *P*-induced evolution of the large erionite-cage diameters O1-O1 and O3-O6 (Tab. S5, Fig. S2b, S3a-b), and the average diameter κ (Tab. S4 and Fig. 5d), are also reported.
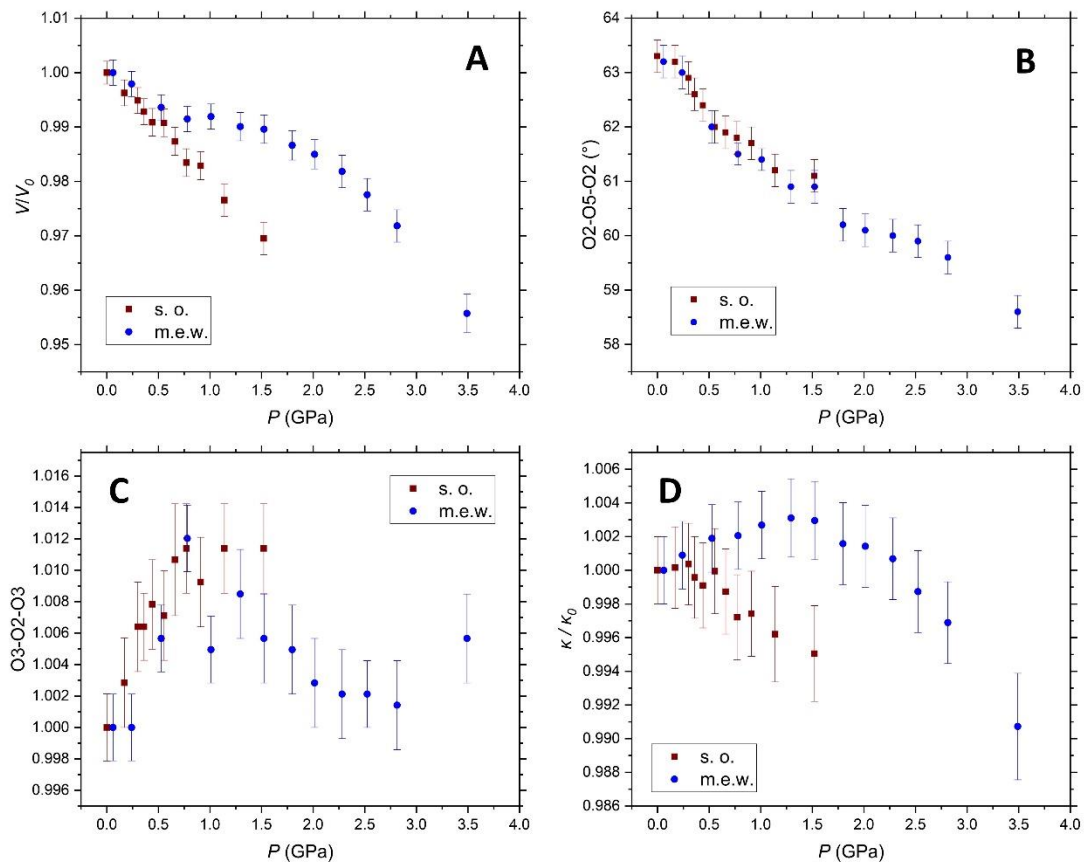
268

Fig. 5: *P*-induced evolution of the: (A) erionite-cage volume, normalized to ambient-*P* values; (B) O2-O5-O2 opening angle of the cancrinite-cage (see Fig. 1b); (C) O3-O2-O3 angle of the D6R, normalized to ambient-*P* values (see Figure S2b); (D) κ average diameter of the erionite-cage, normalized to ambient-*P* values (see section 4.2).

269   **5) Discussion**

270   *5.1) High-pressure elastic and structural behavior*

271   The compressional data obtained from the experiment using the non-penetrating s.o. allow to

272   describe the intrinsic elastic behavior of natural erionite. The refined bulk modulus, $K_{V0} = 47(2)$ GPa,

273   lies in the range of the previously reported zeolites bulk moduli ($\sim 10 < K_{P0,T0} < \sim 90$ GPa, [6]), and

274   is similar to that of other species classified as "zeolites with six-membered rings", *e.g.*, levyne, 56(4)

275   and 48(1) GPa (for $P < \sim 1$ GPa and $P > \sim 1$ GPa), cancrinite, 45(2) GPa, and AlPO-34, 54(3) GPa

276   [4,41,42].

277   As previously reported [5,6,43], the main mechanism of pressure-induced deformation in

278   microporous compounds is the tilting of the quasi-rigid framework building units (*i.e.,* the Al/Si

279   tetrahedra) around the shared oxygen hinges, while the bulk compressibility is significantly controlled

280   by the nature and configuration of the extraframework content, which in turn governs the

281   channels/cavities compression. Concerning the erionite structural response to the applied pressure,

282   the deformation initially involves mainly the tilting of the tetrahedra of the cancrinite cage and of the

283   D6R. In particular, an abrupt decrease of the value of the O2-O5-O2 angle (Fig. 1b, 5b), and a

284   consequent increase of O2-O3-O4 (Fig. 1b, S3c), is observed in the range between 0.00-0.44(5) GPa.

285   In addition, an increase of the di-trigonal distortion of the 6mR (O3-O2-O3, Fig. 5c, S2b), observed

286   both in m.e.w. and s.o., can be reported in the same pressure range. The tilting of the tetrahedra results

287   in the almost horizontal trend of the O1-O1 independent diameter of the erionite-cage (Fig S3b, S2b,

288   blue dashed line). This peculiar deformation of the 6mR (Fig. 5c, S2b) seems to reach a saturated

289   configuration in silicone oil at $\sim 0.70(5)$ GPa, while in m.e.w. an inversion of the trend is observed at

290   the same pressure value, up to a partial recover of the original shape at 2.90(5) GPa. It is interesting

291   to observe that in synthetic K-AlSi-L zeolite and natural cancrinite, compressed in non-penetrating

292   fluids, the same increase in the di-trigonal distortion of the 6mR was reported [41,44]. In contrast, K-

293   AlSi-L in m.e.w. displays an opposite distortion [44], starting from ambient conditions. This

294   mechanism of structural distortion, observed also on natural erionite, might be ascribed to the *P*-

295   induced intrusion of molecules within the channel (in K-AlSi-L framework) or in the erionite-cage,

296   surrounding the cancrinite cage. The decrease in compressibility of the two volumes/structural voids

297   is expected to affect the deformation mechanisms of the adjacent 6mR.

298   In s.o., the volume of the erionite cage decreases almost monotonically all over the

299   investigated pressure range (Fig. 5a). However, different mechanisms can be described at different

300   pressures: in the lower *P*-range (0.0-0.4 GPa), the higher compressibility is shown by the truncated

301   cones of the erionite cage (*i.e.,* Tc1 and Tc2, Fig. S4, S4), both directly affected by the evolution of

302   the D6R/cancrinite-cage channel, rather than the central cylinder (Fig. S4). The compression of the

303   O1-O1 and O3-O6 diameters of the erionite cage on the (0001) plane increases in magnitude at ~ 0.5

304   GPa (Fig S2b, S3a-b, Tab. S5), when the re-arrangement of the cancrinite-cage/D6R channel

305   weakens, as shown by the evolution of O2-O5-O2 (Fig. 1b, 5b, Tab. S4). These mechanisms are

306   responsible for the increase in bulk compressibility observed above that pressure. A similar structural

307   evolution is observed also in m.e.w., where, however, the intrusion of new molecules into the erionite-

308   cage (discussed later) drastically decreases its compressibility, at least up to 1.5 GPa, if compared to

309   silicone oil (Fig 5b, Table S4). No significant re-arrangements involve the extraframework cations

310   and molecules.

311   *5.2) P-induced crystal-fluid interactions*

312   As already described in the literature, *e.g.* [4–7] for reviews, among the main factors controlling the

313   bulk compressibility of a microporous compound, such as a zeolite, the extraframework population

314   plays a key role. Therefore, experiments on the *P*-induced crystal-fluid interactions in synthetic or

315   natural zeolites [28,29,31] have shown that the intrusion of molecules (or monoatomic species) within

316   the structural cavities leads to a sort of "pillar" effect, resulting in a lower bulk compressibility with

317   respect to the intrinsic compressional behavior (*i.e.,* determined by compression in a non-penetrating

318   PTF). The analysis of the *P-V* trends reported in Figure 2a unambiguously suggests that a *P*-induced

319   intrusion of molecules occurred in all the experiments, except that in which silicone oil is used, which

320   is representative of the intrinsic compressional behavior of the natural erionite. Despite the different

321   compressibilities, no discontinuities in the P-V trends were detected in all the experiments. As

322   reported by Gatta and Lee [7], over-hydration in zeolitic compounds without the occurrence of new

323   extraframework sites, $e.g.$, in boggiste and gismondine compressed in m.e.w. [45,46], does not

324   involve a discontinuity in the P-V trend. In the investigated natural erionite, no residual electron

325   densities assignable to new crystallographic positions were detected from the structure refinements

326   of the experiments using potentially penetrating fluids: molecules intrusion involves already existing,

327   and partially occupied, extraframework sites. The refined bulk moduli obtained from penetrating

328   PTFs experiments provide only a qualitative picture of the effect of crystal-fluid interaction on the

329   bulk compressibility ($K_{V0} = \beta_{V0}^{-1}$) of erionite. In particular, it emerges that the compressibility appears

330   to be governed by the water content of the PTF (H_2O wt%: pure-H_2O > m.e.w. > n.h. glyc.). Therefore,

331   it might be concluded that the higher the H_2O content of the PTF, the lower the zeolite

332   compressibility, in response to the higher magnitude of the P-mediated adsorption. The experiment

333   in n.h. glyc. deserves a supplement of discussion. Structure refinements from this experiment (n.h.

334   glyc.) do not show the intrusion of molecules populating the Ow12 site, which shares the same

335   coordinates with the Mg site. However, the overall occupancies of the H_2O-oxygen sites shown in

336   Fig. 4 is only slightly lower with respect to m.e.w, implying a higher occupancy at the H_2O-oxygen

337   sites already occurring at ambient conditions ($i.e.$, Ow7, Ow8, Ow9, Ow10 and Ow11). Moreover, a

338   residue in the difference-Fourier map of the electron density can be observed in the refinements of

339   the n.h. glyc. ramp at 0.66(5) GPa (Fig. 3b). The occurrence of this residue appears to be responsible

340   for the concomitant expansion along the a crystallographic axis (Fig. 2b). We are inclined to believe

341   that this residue may be ascribed to intruded H_2O molecules from the naturally-hydrated glycerol,

342   despite an unambiguous conclusion in this respect cannot be drawn. A question is still open: if this

343   residue reflects the penetration of H_2O molecules only, why is it not observed even in the other

344   experiments in m.e.w. or in distilled water? Can it be rather the effect of glycerol penetration?

345 Furthermore, it is worth to note that the refined fraction of offretite intergrowths in the erionite crystal

346 used for the n.h. glyc. experiment is slightly higher with respect to the other crystals (*i.e.*, *ca.* 20% *vs.*

347 16 %). As the offretite intergrowths can modify the size of the erionite cages, it is not straightforward

348 to assess if and how its occurrence may influence the observed crystal-fluid interaction in natural

349 erionite.

350   In the description of crystal-fluid interaction phenomena, it is important to constrain the

351 pressure range at which it occurs. As reported by Comboni et al. [8] for methanol-MFI interaction,

352 evidence of P-induced adsorption of molecules was already detected at $P < 1$ MPa (*i.e.,* pressures that

353 can be reached in industrial processes). In natural zeolites as well, *e.g.*, boggiste, heulandite and

354 stilbite [45,47,48], adsorption phenomena have been described at $P < 1$ GPa. In natural erionite, the

355 molecules intrusion appears to take place in the range 0.2-0.5 GPa. This is also shown by the P-V

356 evolution of the erionite-cage, corresponding to the zeolitic cavity where new extraframework

357 molecules can be efficiently hosted, as the full occupancy of the K1 site in the cancrinite-cage

358 prevents any intrusion within the cancrinite-cage/D6R channel. As shown in Fig. 5a, at the

359 aforementioned pressures, an unambiguous and significant decrease in compressibility can be

360 observed up to ~ 2.0 GPa. Above this pressure, two mutually related phenomena take place: the

361 saturation of the increasing trend of the overall H_2O-oxygen content, determined according to the

362 refinement strategy described in section 3, (Fig. 4) and a new increase in compressibility of the

363 erionite-cage.

364   It is worth to mention the high-pressure behavior of κ, which is the average diameter on the

365 (0001) plane of the erionite cage (Fig. 5d, Tab. S4). In silicone oil, an unambiguous compression

366 occurs starting from *ca.* 0.5 GPa, while in m.e.w. an expansion is observed up to 1.5 GPa, followed

367 by a compression. This behavior represents a further indirect evidence that the intrusion of molecules

368 involves the erionite cage and occurs in the P-range from 0.0001 to 1.5 GPa. On the contrary, the

369 high-pressure evolution of the interatomic distances and angles of the cancrinite cage and D6R, from

370 the silicone oil and m.e.w. experiments, are almost perfectly overlapped (Figs. 5b, S3c and Tables

371 S4, S5), suggesting that these building units do not actively participate to the crystal-fluid interaction

372 processes.

373   If we compare the crystal-fluid interaction results of this study with those previously obtained

374 with other natural and synthetic zeolites, by means of *in situ* high-*P* single crystal XRD data, *e.g.*,

375 stilbite and AlPO$_4$-5 (STI, and AFI framework types) [28,47] (Fig. 6), we can make a semi-

376 quantitative estimation of the magnitude of the *P*-induced intrusion phenomena. The selected

377 framework-types, according to the Database of Zeolite Structure of the IZA [36], share a similar

378 "accessible volume": 15.10%, 14.07% and 13.27%, respectively for ERI, STI and AFI framework,

379 where the accessible volume represents the portion of the volume that can be occupied by ions and

380 molecules having a continuity between adjacent unit cells. The *P-V* data evolution with non-

381 penetrating and potentially penetrating PTFs shows that the magnitude of the *P*-induced adsorption

382 phenomena in natural erionite appears much more comparable with that observed in the synthetic

383 AlPO$_4$-5 (Fig. 6) than that observed in natural stilbite, for example (Fig. 6).
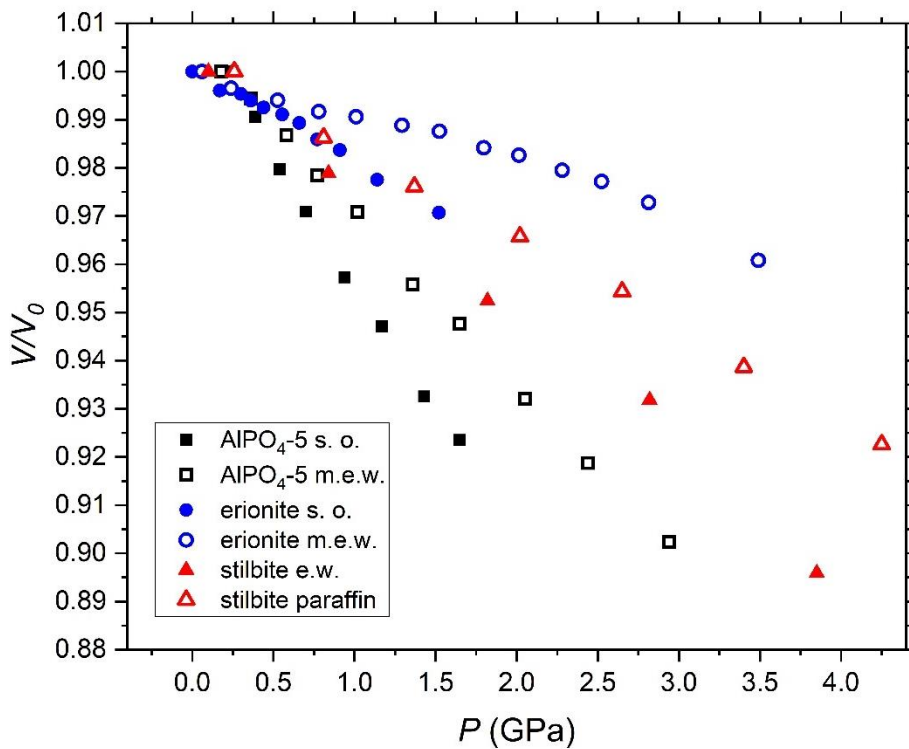

Fig. 6: *P*-induced evolution of the normalized unit-cell volumes of the natural erionite of this study *vs* synthetic AlPO$_4$-5[28] and natural stilbite [46], compressed in different fluids.

384

385   This result is surprising if we consider that the investigated erionite is a natural sample with the

386   cavities significantly filled by the extraframework population, differently from the synthetic $AlPO_4$-

387   5 characterized by almost empty voids. It can also be mentioned that the penetrating PTF used in the

388   stilbite experiments [47] has a nominally higher water content (ethanol:water 4:1) with respect to the

389   m.e.w. mixture (methanol:ethanol:water 16:3:1) used in this study on natural erionite. Further indirect

390   evidence on the magnitude of the crystal-fluid interaction is provided by the comparison of the refined

391   bulk moduli from the non-penetrating silicone oil (intrinsic zeolite compressibility) and from the

392   penetrating fluids experiments. Considering the values from this study (Tab. 2) and those reported in

393   [28,47], we can see that, for example, in natural stilbite, the bulk modulus obtained from the PTF

394   experiment is about 32% higher than that obtained from the non-PTF experiment. In synthetic $AlPO_4$-

395   5 is about 67% higher, while in natural erionite, from this study, the increase in the bulk modulus

396   (*i.e*., the decrease in compressibility) from the m.e.w. experiment with respect to the silicone oil

397   experiment is around 132%.

398   Erionite was also described to occur as an alteration product of oceanic basalts and volcanoclastic

399   sediments [49,50]. It is, therefore, reasonable to suppose that when this zeolite is involved in the early

400   subduction process of the oceanic crust, the increase in pressure (and temperature) and the interaction

401   with the circulating fluids may induce (*P*,*T*)-mediated adsorption of molecules or solvated ions.

402   Considering the new findings described in this manuscript, erionite might be assessed among the most

403   active zeolites governing the fluids migration related to these geological processes. However, it is

404   worth to mention that these hypotheses would require an experimental investigation at in situ high-*P*

405   and high-*T* conditions, to determine the combined influence of pressure and temperature on the

406   crystal-fluid interactions mechanisms.

407   **6) Concluding remarks**

408   In this study, the high-pressure behavior of a natural erionite has been investigated, for the first time,

409   by *in situ* single crystal X-ray diffraction, using both non penetrating (silicone oil) and potentially

penetrating (16:3:1 methanol:ethanol:water mixture, naturally-hydrated glycerol and pure H_2O) P-transmitting fluids.

The isothermal elastic behavior of natural erionite has been modelled by means of a II-order Birch-Murnaghan equation of state, based on the silicone oil data in the range P_{amb}-1.52(5) GPa, yielding a bulk modulus $K_{V0} = 47(2)$ GPa ($\beta_{V0} = 0.0213(9)$ GPa^{-1}). The high-P experiments performed using the potentially penetrating fluids unambiguously show the occurrence of the P-induced intrusion of molecules (Gatta et al. 2018 for a review), which lead to a lower bulk compressibility of erionite due to the "pillar effect" exerted by the intruded molecules. The intrusion likely involves the erionite cage and takes place at relatively low pressure ($P \sim 0.2$ GPa) with increasing its magnitude at higher pressure, whereas the cancrinite cage appears to be unaffected by the crystal-fluid interaction. The anomalous expansion on the (0001) plane, observed in the naturally-hydrated glycerol experiment, may be ascribed to the intrusion of H_2O molecules in a new crystallographic site at the intersection among adjacent erionite cages, even though further investigations are required to validate unambiguously this finding. Finally, a comparison with the reported crystal-fluid interactions in other natural and synthetic zeolites shows that the magnitude of the intrusion phenomena observed in this study is surprisingly high for a natural zeolite. These results disclose interesting scenarios, making natural erionite, a relatively common zeolite, a promising candidate for tailoring crystal-fluid interaction processes having potential technological and industrial applications [5,8,9] and even to investigate the role of zeolites as fluids carriers in early subduction environments, given the reported presence of erionite in altered oceanic basalts and sediments [49,50].

Appendix

The erionite cage, shown in Figure S4, has been modelled as a regular solid shape made by the sum of truncated cones (Tc1, in gold, and Tc2, in red) and a central cylinder (C, in blue). The resulting volume can be modelled as the sum of the volumes of the mentioned solid shapes. As the volume of

435   a cylinder is given by $V_C = \pi \cdot r^2 \cdot h$ (where r is the radius of the basis and h is the height of the cylinder)

436   and the volume of a truncated cone is $V_{TC} = [\pi \cdot h \cdot (r_1^2 + r_1 \cdot r_2 + r_2^2)]/3$ (where h is the height of the

437   truncated cone and r_1 and r_2 the radii of the two bases), the volume of the so-modelled erionite-cage

438   can be obtained according to the following formulae:

439     $V_{ERI\text{-}cage} = V_C + 2 \cdot V_{Tc1} + 2 \cdot V_{Tc2}$

440     $V_C = \pi \cdot (R_C)^2 \cdot h_C$

441     $V_{Tc1} = [\pi \cdot h_{Tc1} \cdot (R_{Tc1}^2 + R_{Tc1} \cdot r_{TC1} + r_{TC1}^2)]/3$

442     $V_{Tc2} = [\pi \cdot h_{Tc2} \cdot (R_{Tc2}^2 + R_{Tc2} \cdot r_{TC2} + r_{TC2}^2)]/3$

443     $R_C = R_{Tc1} = [(O1\text{-}O1 + O3\text{-}O6)/2]/2$: where O1-O1 and O3-O6 are the independent diameters

444   corresponding to both the basis of the cylinder C and the largest basis of the truncated cone TC1;

445     $h_C = O4\text{-}O4$, *i.e.* the height of the cylinder C;

446     $r_{Tc1} = R_{Tc2} = [(O1\text{-}O1)/2]/2$: where O1-O1 is the diameter corresponding to both the smallest basis of

447   the truncated cone Tc1 and the largest basis of the truncated cone Tc2;

448     $h_{Tc1} = c^*z(O1)$: where c corresponds to the unit-cell c parameter and $z(O1)$ is the z coordinate of the

449   O1 atom. Since $z(O4) = 0$, $z(O1)$ can be directly used to calculate the height of the Tc1 truncated cone

450   (see Figure S4).

451     $r_{Tc2} = [(O5\text{-}O6)/2]/2$: where O5-O6 is the diameter of the 6mR corresponding to the smaller basis of

452   the truncated cone Tc2.

453   h_{Tc2}: $[c^*z(O5) + c^*z(O6)]/2 - hTc1$: where c corresponds to the unit-cell c parameter, $z(O5)$ is the z

454   coordinated of the O5 atom and $z(O6)$ the z coordinate of the atom O6 (see Figure S4).

455

462

463

References

[1] Y. Li, J. Yu, Emerging applications of zeolites in catalysis, separation and host–guest assembly, Nat. Rev. Mater. 6, (2021), 1156–1174, https://doi.org/10.1038/s41578-021-00347-3

[2] Y. Li, L. Li, J. Yu, Applications of Zeolites in Sustainable Chemistry, Chem. 3, (2017), 928–949, https://doi.org/10.1016/j.chempr.2017.10.009

[3] J. Zhang, L. Wang, B. Zhang, H. Zhao, U. Kolb, Y. Zhu, L. Liu, Y. Liu, G. Wang, C. Wang, D. Sheng Su, B.C. Gates, F.S. Xiao, Sinter-resistant metal nanoparticle catalysts achieved by immobilization within zeolite crystals via seed-directed growth, Nat. Catal. 1, (2018), 540–546, https://doi.org/10.1038/s41929-018-0098-1

[4] G.D. Gatta, A comparative study of fibrous zeolites under pressure, Eur. J. Mineral. 17, (2005), 411-421, https://doi.org/10.1127/0935-1221/2005/0017-0411

[5] G.D. Gatta, Does porous mean soft? On the elastic behaviour and structural evolution of zeolites under pressure, Z. Kristallogr. 223, (2008), 160–170, https://doi.org/10.1524/zkri.2008.0013

[6] G.D. Gatta, P. Lotti, G. Tabacchi, The effect of pressure on open-framework silicates: elastic behaviour and crystal–fluid interaction, Phys. Chem. Minerals 45, (2018), 115–138, https://doi.org/10.1007/s00269-017-0916-z

[7] G.D. Gatta, Y. Lee, Zeolites at high pressure: A review, Mineral. Mag. 78, (2014), 267–291, https://doi.org/10.1180/minmag.2014.078.2.04

[8] D. Comboni, F. Pagliaro, P. Lotti, G.D. Gatta, M. Merlini, S. Milano, M. Migliori, G. Giordano, E. Catizzone, I.E. Collings, M. Hanfland, The elastic behavior of zeolitic frameworks: The case of MFI type zeolite under high-pressure methanol intrusion, Catalysis Today 345, (2020), https://doi.org/10.1016/j.cattod.2019.10.007

[9] E. Fois, A. Gamba, G. Tabacchi, R. Arletti, S. Quartieri, G. Vezzalini, The "template" effect of the extra-framework content on zeolite compression: The case of yugawaralite, Am. Mineral. 90, (2005), 28–35, https://doi.org/10.2138/am.2005.1653

[10] E. Passaglia, G. Artioli, A. Gualtieri, Crystal chemistry of the zeolites erionite and offretite, Am. Mineral. 83, (1998), 577–589, https://doi.org/10.2138/am-1998-5-617

[11] A.S. Eakle, Erionite, a new zeolite, Am. Journal of Science 156, (1898), 66–68, https://doi.org/10.2475/ajs.s4-6.31.66

[12] A. Gualtieri, G. Artioli, E. Passaglia, S. Bigi, A. Viani, J.C. Hanson, Crystal structure-crystal chemistry relationships in the zeolites erionite and offretite, Am. Mineral. 83, (1998), 590–606, https://doi.org/10.2138/am-1998-5-618

[13] D.S. Coombs, A. Alberti, T. Armbruster, G. Artioli, C. Colella, E. Galli, J.D. Grice, F. Liebau, J.A. Mandarino, H. Minato, E.H. Nickel, E. Passaglia, D.R. Peacor, S. Quartieri, R. Rinaldi, M. Ross, R.A. Sheppard, E. Tillmanns, G. Vezzalini, Recommended nomenclature for zeolite minerals: report of the subcommittee on zeolites of the International Mineralogical Association, Commission on New Minerals and Mineral Names, Can. Mineral. 35, (1997), 1571–1606.

[14] R.A. Sheppard, A.J. Gude, E.L. Munson, Chemical composition and physical properties of the related zeolites offretite and erionite, Am. Mineral. 50, (1965), 244–249.

[15] A. Alberti, A. Martucci, E. Galli, G. Vezzalini, A reexamination of the crystal structure of erionite, Zeolites 19, (1997), 349–352, https://doi.org/10.1016/S0144-2449(97)00102-4

[16] G. Gottardi, E. Galli, Natural Zeolites, Minerals and Rocks Series Vol. 18, Geological Magazine 123(6), (1985), 409 pp, https://doi.org/10.1017/S0016756800024456

[17] T. Armbruster, M.E. Gunter, Natural Zeolites: Occurrence, Properties, Applications, Reviews in Mineralogy & Geochemistry 45 (D.L. Bish and D.W. Ming, editors), (2001), pp 1–57

[18] J.L. Schlenker, J.J. Pluth, J.V. Smith, Dehydrated natural erionite with stacking faults of the offretite type, Acta Cryst. B33, (1977), 3265–3268, https://doi.org/10.1107/S0567740877010784

[19] Monographs on the evaluation of carcinogenic risks to humans, Arsenic, Metals, Fibres and Dusts 100C, Published by International Agency for Research on Cancer, Lyon, France, (2012), pp 311–316

[20] M. Guinset, J.P. Gilson, Catalytic Science Series (Ed G.J. Hutchings) 3, Introduction to Zeolites Science and Technology, (2002), pp 1–29

[21] J. Tekla, L. Lakiss, V. Valchev, K.A. Tarach, M. Jablonska, V. Girman, A. Szymocha, A. Kowalczyk, K. Gora-Marek, J.P. Gilson, Increasing the catalytic performance of erionite by hierarchization, Microporous Mesoporous Mater. 229, (2020), https://doi.org/10.1016/j.micromeso.2020.110088

[22] J. Zhu, V.L. Sushkevich, A.J. Knorpp, M.A. Newton, S.C.M. Mizuno, T. Wakihara, T. Okubo, Z. Liu, J.A. Van Bokhoven, Cu-Erionite Zeolite Achieves High Yield in Direct Oxidation of Methane to Methanol by Isothermal Chemical Looping, Chem. Mater. 32, (2020), 1448–1453, https://dx.doi.org/10.1021/acs.chemmater.9b04223

[23] G. Cametti, S.V. Churakov, Crystal structure of Ag-exchanged levyne intergrown with erionite: Single-crystal X-ray diffraction and Molecular Dynamics simulations, Am. Mineral. 105, (2020), 1631–1638, https://doi.org/10.2138/am-2020-7500

[24] H.F. Chen, Y.J. Lin, B.H. Chen, I. Yoshiyuki, S.Y.H. Liou, R.T. Huang, A Further Investigation of NH4+ Removal Mechanisms by Using Natural and Synthetic Zeolites in Different Concentrations and Temperatures, Minerals 8, (2018), https://doi.org/10.3390/min8110499

[25] P. Ballirano, G. Cametti, Dehydration dynamics and thermal stability of erionite-K: Experimental evidence of the "internal ionic exchange" mechanism, Microporous Mesoporous Mater. 163, (2012), 160–168, http://dx.doi.org/10.1016/j.micromeso.2012.06.059

[26] P. Ballirano, A. Pacella, Erionite-Na upon heating: dehydration dynamics and exchangeable cations mobility, Sci. Rep. 6, (2016), https://doi.org/10.1038/srep22786

[27] P. Ballirano, A. Bloise, C. Cremisini, E. Nardi, M.R. Mentereali, A. Pacella, Thermally induced behavior of the K-exchanged erionite: a further step in understanding the structural modifications of the erionite group upon heating Periodico di Mieralogia, (2018), 123–134, https://doi.org/10.2451/2018PM769

[28] P. Lotti, G.D. Gatta, D. Comboni, M. Merlini, L. Pastero, M. Hanfland, AlPO4-5 zeolite at high pressure: Crystal–fluid interaction and elastic behavior, Microporous Mesoporous Mater. 228, (2016), 158–167, http://dx.doi.org/10.1016/j.micromeso.2016.03.030

[29] P. Lotti, R. Arletti, G.D. Gatta, S. Quartieri, G. Vezzalini, M. Merlini, V. Dmitriev, M. Hanfland, Compressibility and crystal–fluid interactions in all-silica ferrierite at high pressure, Microporous Mesoporous Mater. 218, (2015), 42–54, http://dx.doi.org/10.1016/j.micromeso.2015.06.044

[30] D. Comboni, G.D. Gatta, P. Lotti, M. Merlini, H.P. Liermann, On the P-induced behavior of the zeolite phillipsite: an in situ single-crystal synchrotron X-ray diffraction study Phys. Chem. Minerals 44, (2017) 1–20, https://doi.org/10.1007/s00269-016-0832-7

[31] D. Comboni, G.D. Gatta, P. Lotti, M. Merlini, M. Hanfland, Crystal-fluid interactions in laumontite, Microporous Mesoporous Mater. 263, (2018), 86–95, https://doi.org/10.1016/j.micromeso.2017.12.003

[32] Rigaku Oxford Diffraction, CrysAlisPro Software system, version 1.171.40.67a, Rigaku Corporation, (2019) Wroclaw, Poland.

[33] H.K. Mao, J. Xu, P.M. Bell, Calibration of the ruby pressure gauge to 800 kbar under quasi-hydrostatic conditions, J. Geophys. Res. 91, (1986), 4673–4676, https://doi.org/10.1029/JB091iB05p04673

[34] J.C. Chervin, B. Canny, M. Mancinelli, Ruby-spheres as pressure gauge for optically transparent high pressure cells, High Press. Res. 21, (2001), 302–314, https://doi.org/10.1080/08957950108202589

[35] R.J. Angel, M. Bujak, J. Zhao, G.D. Gatta, S.D. Jacobsen, Effective hydrostatic limits of pressure media for high-pressure crystallographic studies, J. Appl. Crystallogr. 40 (2007), 26–32, https://doi.org/10.1107/S0021889806045523

[36] C. Baerlocher, L.B. McCusker, D.H. Olson, Atlas of zeolite framework types, sixth revised ed., Elsevier, Amsterdam, 2007

[37] M. Merlini, M. Hanfland, Single-crystal diffraction at megabar conditions by synchrotron radiation, High Press. Res. 33, (2013), 511–522, https://doi.org/10.1080/08957959.2013.831088

[38] V. Petricek, M. Dusek, L. Palatinus, Crystallographic Computing System JANA2006: General features, Z. Kristallogr. 229, (2014), 345e352, https://doi.org/10.1515/zkri-2014-1737

[39] R.J. Angel, Equations of State, Rev. Mineral. Geochem. 41, (2000), 35–60, https://doi.org/10.1515/9781501508707-006

[40] R.J. Angel, M. Alvaro, J. Gonzalez-Platas, EosFit7c and a Fortran module (library) for equation of state calculations, Z. Kristallogr. 229 (2014) 405–419, https://doi.org/10.1515/zkri-2013-1711

[41] P. Lotti, G.D. Gatta, N. Rotiroti, F. Camara, High-pressure study of a natural cancrinite, Am. Mineral. 97, (2012), 872–882, http://dx.doi.org/10.2138/am.2012.4039

[42] L. Leardini, S. Quartieri, A. Martucci, G. Vezzalini, V. Dmitriev, Compressibility of microporous materials with CHA topology: 2. ALPO-34, Zeitschrift für Kristallographie - Crystalline Materials 227, (2012), 514–521, https://doi.org/10.1524/zkri.2012.1477

[43] G.D. Gatta, Extreme deformation mechanisms in open-framework silicates at high-pressure: Evidence of anomalous inter-tetrahedral angles, Microporous Mesoporous Mater. 128, (2010), 78–84, https://doi.org/10.1016/j.micromeso.2009.08.006

[44] L. Gigli, G. Vezzalini, S. Quartieri, R. Arletti, Compressibility behavior and pressure-induced over-hydration of zeolite Ksingle bondAlSi-L, Microporous Mesoporous Mater. 276, (2019), 160–166, https://doi.org/10.1016/j.micromeso.2018.09.031

[45] R. Arletti, S. Quartieri, G. Vezzalini, Elastic behavior of zeolite boggsite in silicon oil and aqueous medium: A case of high-pressure-induced over-hydration, Am. Mineral. 95, (2010), 1247–1256, https://doi.org/10.2138/am.2010.3482

[46] S. Ori, S. Quartieri, G. Vezzalini, V. Dmitriev, Pressure-induced over-hydration and water ordering in gismondine: A synchrotron powder diffraction study, Am. Mineral. 93, (2008), 1393–1403, https://doi.org/10.2138/am.2008.2838

[47] Y.V. Seryotkin, S.N. Dementiev, A.Y. Likhacheva, Crystal–fluid interaction: the evolution of stilbite structure at high pressure, Phys. Chem. Minerals 48, (2021), 1–11, https://doi.org/10.1007/s00269-020-01131-5,

[48] Y.V. Seryotkin, Microporous Mesoporous Mater., (2015), 127–135, https://doi.org/10.1016/j.micromeso.2015.05.015

[49] M. Kastner, Marine Minerals, in: R.G. Burns (Ed.), Reviews in Mineralogy 6, Mineralogical Society of America, Chantilly, 1979, pp. 111-122.

[50] R.L. Hay, R.A. Sheppard, Natural Zeolites: Occurrence, Properties, Applications, in: D.L. Bish, D.W. Ming (Eds.) Reviews in Mineralogy and Geochemistry 45, Mineralogical Society of America, Chantilly, 2001, pp. 217-234.

Experiment	Unique reflections	Observed reflections $I > 3\sigma(I)$	Refined variables	R_1 (obs)	wR_1 (obs)	R_1 (all)	wR_1 (all)
In air	965	595	82	0.0644	0.0804	0.1109	0.0865
s. o. P_0	1670	1119	48	0.1045	0.1341	0.1314	0.1368
" P_1	1330	989	47	0.1040	0.1478	0.1234	0.1584
" P_2	1292	968	47	0.1027	0.1433	0.1177	0.1448
" P_3	1298	962	47	0.1034	0.1435	0.1201	0.1451
" P_4	1295	988	47	0.1027	0.1468	0.1177	0.1482
" P_5	1298	970	47	0.1058	0.1527	0.1218	0.1546
" P_6	1299	978	47	0.1104	0.1565	0.1278	0.1597
" P_7	1291	1011	47	0.1118	0.1628	0.1263	0.1646
" P_8	1285	1000	47	0.1106	0.1567	0.1256	0.1583
" P_9	1281	972	47	0.1244	0.1747	0.1421	0.1764
" P_{10}	1279	970	47	0.1248	0.1752	0.1426	0.1770
m.e.w. P_0	1457	1038	48	0.1026	0.1294	0.1256	0.1322
" P_1	1606	1182	47	0.0999	0.1304	0.1191	0.1329
" P_2	1595	1206	47	0.1019	0.1332	0.1172	0.1350
" P_3	1576	1205	48	0.1054	0.1326	0.1197	0.1339
" P_4	1568	1192	49	0.1052	0.1318	0.1194	0.1331
" P_5	1574	1194	49	0.1111	0.1442	0.1257	0.1435
" P_6	1556	1179	49	0.1108	0.1422	0.1270	0.1437
" P_7	1562	1201	49	0.1148	0.1497	0.1294	0.1510
" P_8	1562	1176	49	0.1159	0.1503	0.1327	0.1519
" P_9	1544	1155	49	0.1137	0.1485	0.1310	0.1499
" P_{10}	1549	1151	49	0.1170	0.1527	0.1344	0.1542
" P_{11}	1538	1139	49	0.1175	0.1529	0.1358	0.1545
" P_{12}	1522	1111	49	0.1174	0.1505	0.1354	0.1523
" P_{13}	1331	968	49	0.1244	0.1619	0.1442	0.1642
" P_{14}*	1561	1191	49	0.1037	0.1298	0.1189	0.1310
" P_0*	1565	1172	47	0.1014	0.1279	0.1173	0.1293

602

603

Tab. S1 *(continued)*

Experiment	Unique reflections	Observed reflections $I > 3\sigma(I)$	Refined variables	R_1 (obs)	wR_1 (obs)	R_1 (all)	wR_1 (all)
n.h. glyc. P_1	1392	930	48	0.1173	0.1514	0.1478	0.1538
" P_2	1380	915	47	0.1155	0.1445	0.1529	0.1482
" P_3	1383	903	47	0.1141	0.1434	0.1537	0.1473
" P_4	1385	909	47	0.1180	0.1445	0.1552	0.1479
" P_5	1364	910	47	0.1216	0.1512	0.1568	0.1545
" P_6	1367	886	48	0.1291	0.1623	0.1670	0.1659
" P_7	1367	871	48	0.1383	0.1724	0.1757	0.1774
" P_8	1361	860	48	0.1427	0.1783	0.1853	0.1821
" P_9	1397	765	48	0.1396	0.1738	0.1896	0.1765
" P_{10}	1329	790	48	0.1565	0.1916	0.2103	0.1971
" P_{11}	1298	710	48	0.1619	0.1790	0.2274	0.1856
" P_{12}	1270	637	48	0.1750	0.1920	0.2534	0.2006
" P_{13}*	1361	888	48	0.1376	0.1723	0.1704	0.1751
" P_{14}*	1408	833	48	0.1375	0.1728	0.1819	0.1753
" P_0*	1390	894	48	0.1193	0.1486	0.1570	0.1516
pure H_2O P_1	1245	948	48	0.1196	0.1695	0.1352	0.1721
" P_2	1250	961	48	0.1190	0.1741	0.1359	0.1776
" P_3	1248	964	49	0.1198	0.1741	0.1361	0.1775
" P_4	1254	976	49	0.1191	0.1708	0.1352	0.1730
" P_5	1250	955	49	0.1198	0.1754	0.1360	0.1780
" P_6	1249	956	49	0.1215	0.1730	0.1370	0.1759
" P_0*	1267	968	47	0.1207	0.1596	0.1369	0.1623

Experiment		P (GPa)	Ow7	Ow8	Ow9	Ow10	Ow11	Ow12	Ow13
s.o.	P_0	0.0001	0.50(4)	0.30(2)	0.26(2)	0.53(2)	0.21(2)		
"	P_1	0.17(5)	0.31(10)	0.40(3)	0.28(3)	0.45(2)	0.27(4)		
"	P_2	0.30(5)	0.37(5)	0.39(3)	0.27(3)	0.43(2)	0.24(3)		
"	P_3	0.36(5)	0.38(5)	0.44(3)	0.28(2)	0.44(2)	0.24(2)		
"	P_4	0.44(5)	0.35(5)	0.44(3)	0.25(3)	0.44(2)	0.27(3)		
"	P_5	0.55(5)	0.31(6)	0.45(3)	0.26(3)	0.41(3)	0.30(3)		
"	P_6	0.66(5)	0.30(7)	0.51(3)	0.26(3)	0.41(3)	0.30(3)		
"	P_7	0.77(5)	0.30(7)	0.49(3)	0.25(3)	0.40(3)	0.32(3)		
"	P_8	0.91(5)	0.31(7)	0.40(3)	0.14(3)	0.38(3)	0.34(3)		
"	P_9	1.14(5)	0.26(8)	0.44(3)	0.15(3)	0.40(3)	0.34(4)		
"	P_{10}	1.52(5)	0.25(8)	0.44(3)	0.15(3)	0.40(3)	0.35(4)		
m.e.w.	P_0	0.0001	0.43(4)	0.33(3)	0.31(1)	0.53(2)	0.26(2)		
"	P_1	0.06(5)	0.55(4)	0.29(3)	0.40(2)	0.68(2)	0.17(2)		
"	P_2	0.24(5)	0.58(4)	0.32(3)	0.28(2)	0.56(2)	0.22(2)		
"	P_3	0.53(5)	0.73(3)	0.21(3)	0.32(3)	0.43(3)	0.22(2)	0.13(3)	
"	P_4	0.78(5)	0.79(3)	0.33(3)	0.33(3)	0.50(3)	0.30(2)	0.28(3)	0.21(4)
"	P_5	1.01(5)	0.79(3)	0.36(3)	0.34(3)	0.45(3)	0.27(2)	0.46(3)	0.16(4)
"	P_6	1.30(5)	0.85(4)	0.52(3)	0.23(3)	0.57(4)	0.32(3)	0.60(3)	0.23(4)
"	P_7	1.52(5)	0.92(4)	0.53(3)	0.24(4)	0.60(3)	0.32(3)	0.68(3)	0.26(4)

"	P_8	1.80(5)	1.04(3)	0.65(3)	0.21(3)	0.70(3)	0.17(3)	0.92(3)	0.15(4)
"	P_9	2.01(5)	0.99(3)	0.65(3)	0.18(3)	0.72(4)	0.18(3)	0.98(3)	0.15(4)
"	P_{10}	2.28(5)	1.05(3)	0.70(3)	0.18(3)	0.72(3)	0.16(3)	1.02(3)	0.17(4)
"	P_{11}	2.52(5)	1.11(3)	0.72(3)	0.17(4)	0.77(4)	0.22(3)	1.01(3)	0.16(4)
"	P_{12}	2.81(5)	1.11(3)	0.72(3)	0.20(4)	0.82(4)	0.27(4)	0.96(3)	0.20(4)
"	P_{13}	3.49(5)	1.06(4)	0.77(3)	0.19(4)	0.82(4)	0.31(3)	0.93(4)	0.29(4)
"	$P_{14}*$	0.47(5)	0.74(3)	0.19(2)	0.36(4)	0.30(3)	0.19(2)	0.13(3)	0.01(3)
"	$P_{15}*$	0.0001	0.59(3)	0.14(2)	0.34(4)	0.25(4)	0.18(2)		
n.h. glyc.	P_1	0.32(5)	0.73(5)	0.33(3)	0.33(3)	0.52(3)	0.21(3)		
"	P_2	0.44(5)	0.67(5)	0.37(3)	0.33(3)	0.57(3)	0.24(3)		
"	P_3	0.52(5)	0.77(4)	0.39(3)	0.23(3)	0.60(3)	0.24(3)		
"	P_4	0.65(5)	0.97(5)	0.52(3)	0.16(3)	0.63(3)	0.14(3)		
"	P_5	0.95(5)	0.90(5)	0.57(3)	0.13(3)	0.66(3)	0.20(3)		
"	P_6	1.43(5)	1.01(5)	0.79(4)	0.20(3)	0.76(3)	0.16(3)		0.14(5)
"	P_7	1.90(5)	1.11(5)	0.82(5)	0.21(3)	0.84(4)	0.23(4)		0.17(5)
"	P_8	2.41(5)	1.19(5)	0.88(4)	0.23(3)	0.88(4)	0.22(3)		0.11(5)
"	P_9	2.93(5)	1.20(5)	0.91(5)	0.27(3)	0.96(3)	0.17(3)		0.16(5)
"	P_{10}	3.43(5)	1.19(5)	0.81(5)	0.27(4)	1.01(4)	0.23(3)		0.07(6)
"	P_{11}	3.96(5)	1.15(5)	0.94(4)	0.30(3)	0.98(3)	0.20(3)		0.13(5)
"	P_{12}	4.49(5)	1.14(5)	0.92(4)	0.32(4)	0.99(4)	0.20(3)		0.22(5)
"	$P_{13}*$	2.06(5)	1.29(5)	0.77(4)	0.16(3)	0.92(4)	0.20(3)		0.27(5)
"	$P_{14}*$	0.54(5)	1.25(5)	0.71(4)	0.17(3)	0.90(4)	0.20(3)		0.39(5)
"	P_0*	0.0001	0.96(5)	0.52(3)	0.19(3)	0.55(3)	0.07(3)		0.20(5)

pure H_2O	P_1	0.16(5)	0.51(5)	0.49(4)	0.25(3)	0.63(3)	0.16(3)		
"	P_2	0.33(5)	0.44(7)	0.37(4)	0.28(3)	0.48(3)	0.30(4)		0.18(6)
"	P_3	0.42(5)	0.39(7)	0.48(4)	0.29(3)	0.54(3)	0.24(4)	0.15(5)	0.13(5)
"	P_4	0.58(5)	0.21(8)	0.48(4)	0.22(3)	0.51(3)	0.27(4)	0.21(5)	0.13(5)
"	P_5	0.74(5)	0.16(13)	0.62(4)	0.27(3)	0.55(4)	0.30(6)	0.33(5)	0.28(5)
"	P_6	0.99(5)	0.53(6)	0.61(4)	0.18(3)	0.61(3)	0.09(3)	0.13(6)	0.12(5)
"	P_0*	0.0001	0.41(5)	0.23(5)	0.29(3)	0.42(4)	0.23(3)		

609

610

611 **Tab. S3:** *P*-induced evolution of the unit-cell parameters of natural erionite compressed in silicone oil, m.e.w.,
612 naturally-hydrated glycerol and pure H_2O (* data collected in decompression).

613

Experiment		P (GPa)	a (Å)	c (Å)	V (Å^3)
s. o.	P_0	0.0001	13.2621(2)	15.0706(3)	2295.5(1)
"	P_1	0.17(5)	13.2510(4)	15.0365(2)	2286.5(1)
"	P_2	0.30(5)	13.2520(4)	15.0231(2)	2284.8(1)
"	P_3	0.36(5)	13.2488(4)	15.0097(2)	2281.7(1)
"	P_4	0.44(5)	13.2457(4)	14.9950(2)	2278.4(1)
"	P_5	0.55(5)	13.2420(4)	14.9817(2)	2275.1(1)
"	P_6	0.66(5)	13.2363(4)	14.9679(2)	2271.0(1)
"	P_7	0.77(5)	13.2231(4)	14.9460(2)	2263.2(1)
"	P_8	0.91(5)	13.2155(4)	14.9296(2)	2258.1(1)
"	P_9	1.14(5)	13.1937(5)	14.8851(3)	2244.0(1)
"	P_{10}	1.52(5)	13.1799(9)	14.8121(5)	2228.3(2)
m.e.w.	P_0	0.0001	13.2581(4)	15.0696(2)	2294.47(5)
"	P_1	0.06(5)	13.2592(2)	15.0604(3)	2292.99(7)
"	P_2	0.24(5)	13.2517(2)	15.0252(3)	2285.04(7)
"	P_3	0.53(5)	13.2537(2)	14.9830(3)	2279.33(8)
"	P_4	0.78(5)	13.2525(2)	14.9500(3)	2273.87(8)
"	P_5	1.01(5)	13.2542(2)	14.9300(3)	2271.44(7)
"	P_6	1.30(5)	13.2531(2)	14.9063(3)	2267.44(7)
"	P_7	1.52(5)	13.2525(2)	14.8886(3)	2264.53(7)
"	P_8	1.80(5)	13.2426(2)	14.8591(3)	2256.66(7)
"	P_9	2.01(5)	13.2393(2)	14.8431(3)	2253.11(7)
"	P_{10}	2.28(5)	13.2286(2)	14.8198(3)	2245.94(8)
"	P_{11}	2.52(5)	13.2220(2)	14.7999(3)	2240.70(7)
"	P_{12}	2.81(5)	13.2064(2)	14.7682(3)	2230.62(8)
"	P_{13}	3.49(5)	13.1618(3)	14.6854(5)	2203.15(9)
"	P_{14}*	0.47(5)	13.2662(2)	14.9968(3)	2285.70(7)
"	P_0*	0.0001	13.2634(2)	15.0782(3)	2297.17(7)

Tab. S3 *(continued)*

Experiment		P (GPa)	a (Å)	c (Å)	V (Å^3)
n.h. glyc.	P_1	0.32(5)	13.2465(3)	15.0568(3)	2288.1(1)
"	P_2	0.44(5)	13.2489(4)	15.0271(3)	2284.4(1)
"	P_3	0.52(5)	13.2552(4)	15.0007(4)	2283.6(1)
"	P_4	0.65(5)	13.2640(3)	14.9831(3)	2282.9(1)
"	P_5	0.95(5)	13.2638(3)	14.9462(3)	2277.2(1)
"	P_6	1.43(5)	13.2507(4)	14.9059(4)	2266.6(1)
"	P_7	1.90(5)	13.2410(4)	14.8726(4)	2258.2(1)
"	P_8	2.41(5)	13.2252(4)	14.8228(4)	2245.3(1)
"	P_9	2.93(5)	13.1956(5)	14.7634(4)	2226.2(1)
"	P_{10}	3.43(5)	13.1553(5)	14.6930(5)	2202.1(1)
"	P_{11}	3.96(5)	13.1029(7)	14.6100(6)	2172.3(2)
"	P_{12}	4.49(5)	13.0525(9)	14.5490(6)	2146.6(2)
"	P_{13}*	2.06(5)	13.2378(4)	14.8494(3)	2253.6(1)
"	P_{14}*	0.54(5)	13.2414(4)	14.8520(4)	2255.2(1)
"	P_0*	0.0001	13.2578(3)	15.0063(4)	2284.3(1)
pure H_2O	P_1	0.16(5)	13.2792(2)	15.0468(2)	2297.85(6)
"	P_2	0.33(5)	13.2799(3)	15.0260(3)	2294.91(7)
"	P_3	0.42(5)	13.2788(2)	15.0108(2)	2292.19(7)
"	P_4	0.58(5)	13.2764(3)	14.9908(3)	2288.30(8)
"	P_5	0.74(5)	13.2785(2)	14.9762(3)	2286.81(7)
"	P_6	0.99(5)	13.2796(2)	14.9591(2)	2284.57(7)
"	P_0*	0.0001	13.2810(2)	15.0657(2)	2301.34(7)

Tab. S4: High-pressure evolution of: *i*) O2-O5-O2 interatomic opening angle of the cancrinite-cage, *ii*) volume of the erionite-cage (see appendix for further details), *iii*) average diameter of the cylindrical volume of the erionite-cage [κ = (O1-O1 + O3-O6)/2], *iv*) O3-O2-O3 angle of the D6R in cancrinite-cage (see Figure S2b) from the silicone oil and m.e.w. experiments.

Experiment		P (GPa)	O2-O5-O2 (°)	$V_{erionite\text{-}cage}(\text{Å}^3)$	κ (Å)	O3-O2-O3 (°)
s. o.	P_0	0.0001	63.3(3)	937(1)	9.50(2)	140.5(3)
"	P_1	0.17(5)	63.2(3)	934(1)	9.50(2)	140.9(4)
"	P_2	0.30(5)	62.9(3)	933(1)	9.50(2)	141.4(4)
"	P_3	0.36(5)	62.6(3)	931(1)	9.49(2)	141.4(3)
"	P_4	0.44(5)	62.4(3)	929(2)	9.49(2)	141.6(4)
"	P_5	0.55(5)	62.0(3)	929(2)	9.50(2)	141.5(4)
"	P_6	0.66(5)	61.9(3)	926(2)	9.49(2)	142.0(5)
"	P_7	0.77(5)	61.8(3)	922(2)	9.47(2)	142.1(4)
"	P_8	0.91(5)	61.7(3)	921(2)	9.47(2)	141.8(4)
"	P_9	1.14(5)	61.2(3)	915(2)	9.46(3)	142.1(4)
"	P_{10}	1.52(5)	61.1(3)	909(2)	9.45(3)	142.1(4)
m.e.w.	P_1	0.06(5)	63.2(3)	934(1)	9.48(2)	141.3(3)
"	P_2	0.24(5)	63.0(3)	933(1)	9.49(2)	141.3(3)
"	P_3	0.53(5)	62.0(3)	929(1)	9.50(2)	142.1(3)
"	P_4	0.78(5)	61.5(3)	927(1)	9.50(2)	143.0(3)
"	P_5	1.01(5)	61.4(3)	927(1)	9.51(2)	142.0(3)
"	P_6	1.30(5)	60.9(3)	925(2)	9.51(2)	142.5(4)
"	P_7	1.52(5)	60.9(3)	925(2)	9.51(2)	142.1(4)
"	P_8	1.80(5)	60.2(3)	922(2)	9.50(2)	142.0(4)
"	P_9	2.01(5)	60.1(3)	921(2)	9.50(2)	141.7(4)
"	P_{10}	2.28(5)	60.0(3)	918(2)	9.49(2)	141.6(4)
"	P_{11}	2.52(5)	59.9(3)	914(2)	9.47(2)	141.6(3)
"	P_{12}	2.81(5)	59.6(3)	908(2)	9.45(2)	141.5(4)
"	P_{13}	3.49(5)	58.6(3)	893(2)	9.40(3)	142.1(4)

615

616

Tab. S5: High-pressure evolution of: *i*) O2-O4-O3 opening angle of the D6R, *ii*) O1-O1 and O3-O6 independent diameters of the erionite cage and *iii*) volumes of the geometrical components (Tc1, Tc2 and C) of the erionite-cage (see appendix for further details).

Experiment		P (GPa)	O2-O4-O3 (°)	O1-O1 (Å)	O3-O6 (Å)	V_{Tc1} (Å³)	V_{Tc2} (Å³)	V_C (Å³)
s.o.	P_0	0.0001	95.4(2)	9.281(9)	9.717(10)	152.5(4)	49.2(3)	533.9(5)
"	P_1	0.17(5)	95.8(2)	9.298(12)	9.703(11)	151.7(5)	48.9(3)	532.9(7)
"	P_2	0.30(5)	96.0(3)	9.306(12)	9.699(11)	151.1(5)	48.9(3)	532.6(7)
"	P_3	0.36(5)	96.1(3)	9.301(12)	9.689(11)	150.8(5)	48.9(3)	531.3(7)
"	P_4	0.44(5)	96.5(3)	9.301(12)	9.680(12)	150.5(5)	48.8(3)	530.3(7)
"	P_5	0.55(5)	96.5(3)	9.292(12)	9.705(12)	150.5(5)	48.5(3)	530.7(7)
"	P_6	0.66(5)	96.7(3)	9.295(12)	9.679(12)	149.9(5)	48.4(4)	528.9(7)
"	P_7	0.77(5)	96.8(3)	9.281(12)	9.664(12)	149.4(5)	48.3(4)	526.5(7)
"	P_8	0.91(5)	96.7(3)	9.275(12)	9.674(12)	149.4(5)	48.2(4)	526.2(7)
"	P_9	1.14(5)	97.2(3)	9.287(13)	9.639(14)	148.3(6)	47.7(4)	523.3(8)
"	P_{10}	1.52(5)	97.0(3)	9.277(13)	9.627(14)	147.2(6)	47.5(4)	519.6(8)
m.e.w.	P_1	0.06(5)	95.7(2)	9.272(9)	9.698(10)	152.4(5)	49.0(3)	532.0(5)
"	P_2	0.24(5)	96.0(2)	9.292(9)	9.695(10)	151.8(5)	48.8(3)	531.7(5)
"	P_3	0.53(5)	97.0(2)	9.313(9)	9.693(10)	150.0(5)	48.7(3)	531.2(5)
"	P_4	0.78(5)	97.4(2)	9.324(9)	9.685(10)	149.7(5)	48.5(3)	530.2(5)
"	P_5	1.01(5)	97.6(2)	9.316(9)	9.705(10)	150.1(5)	48.4(3)	530.2(5)

"	P_6	1.30(5)	98.0(2)	9.328(12)	9.701(10)	149.4(6)	48.4(3)	529.8(6)
"	P_7	1.52(5)	98.2(2)	9.313(12)	9.713(10)	149.6(6)	48.3(3)	529.0(6)
"	P_8	1.80(5)	98.7(2)	9.304(12)	9.696(11)	149.8(6)	48.0(3)	526.5(6)
"	P_9	2.01(5)	98.8(2)	9.302(12)	9.695(11)	149.2(6)	48.2(3)	525.8(6)
"	P_{10}	2.28(5)	99.1(3)	9.292(12)	9.691(11)	148.7(7)	48.0(4)	524.2(6)
"	P_{11}	2.52(5)	99.5(3)	9.273(12)	9.673(11)	148.3(7)	47.8(4)	521.4(6)
"	P_{12}	2.81(5)	99.9(3)	9.251(12)	9.660(11)	147.2(7)	47.8(4)	518.4(6)
"	P_{13}	3.49(5)	100.3(3)	9.200(15)	9.594(15)	144.6(8)	47.5(4)	509.1(8)

620
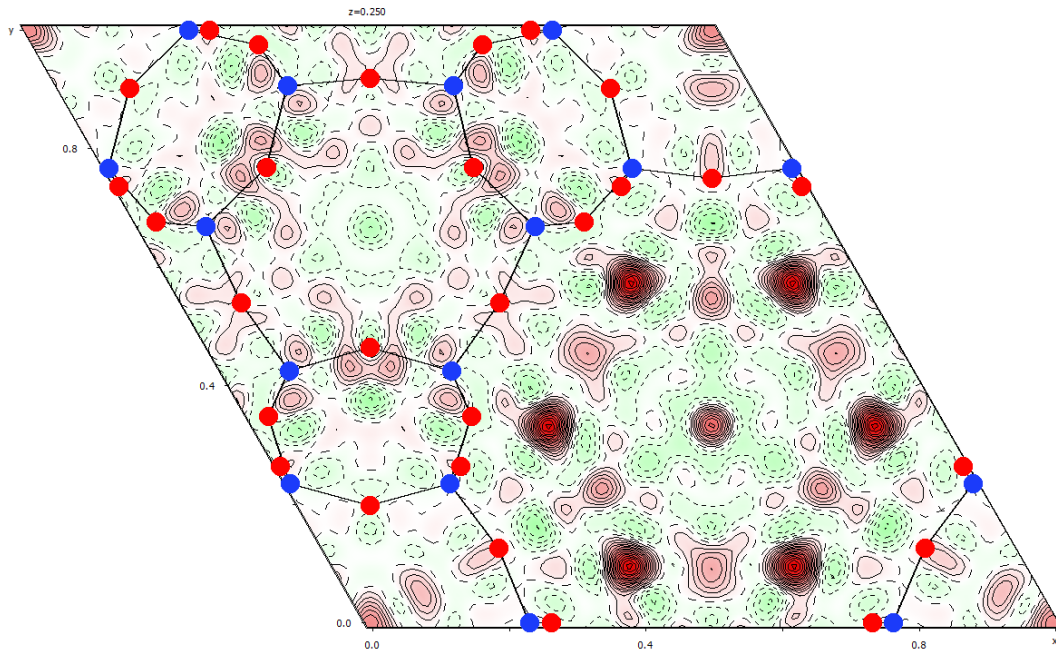
Fig. S1: Residual peaks (green positives and red negatives) in the difference-Fourier maps of electron density, related to the Si and O positions of the offretite framework.

624 **Fig. S2**: (A) The erionite cage and its extraframework content at ambient conditions; (B) section viewed down the *c* axis with D6R from the channel and the adjacent erionite cage: blue dashed line O3-O6 and O1-O1 (two indipendent diameters of C), gold dot line O1-O1 (smaller basis of Tc$_1$) and red dash dot line O5-O6 (smaller basis of Tc$_2$).
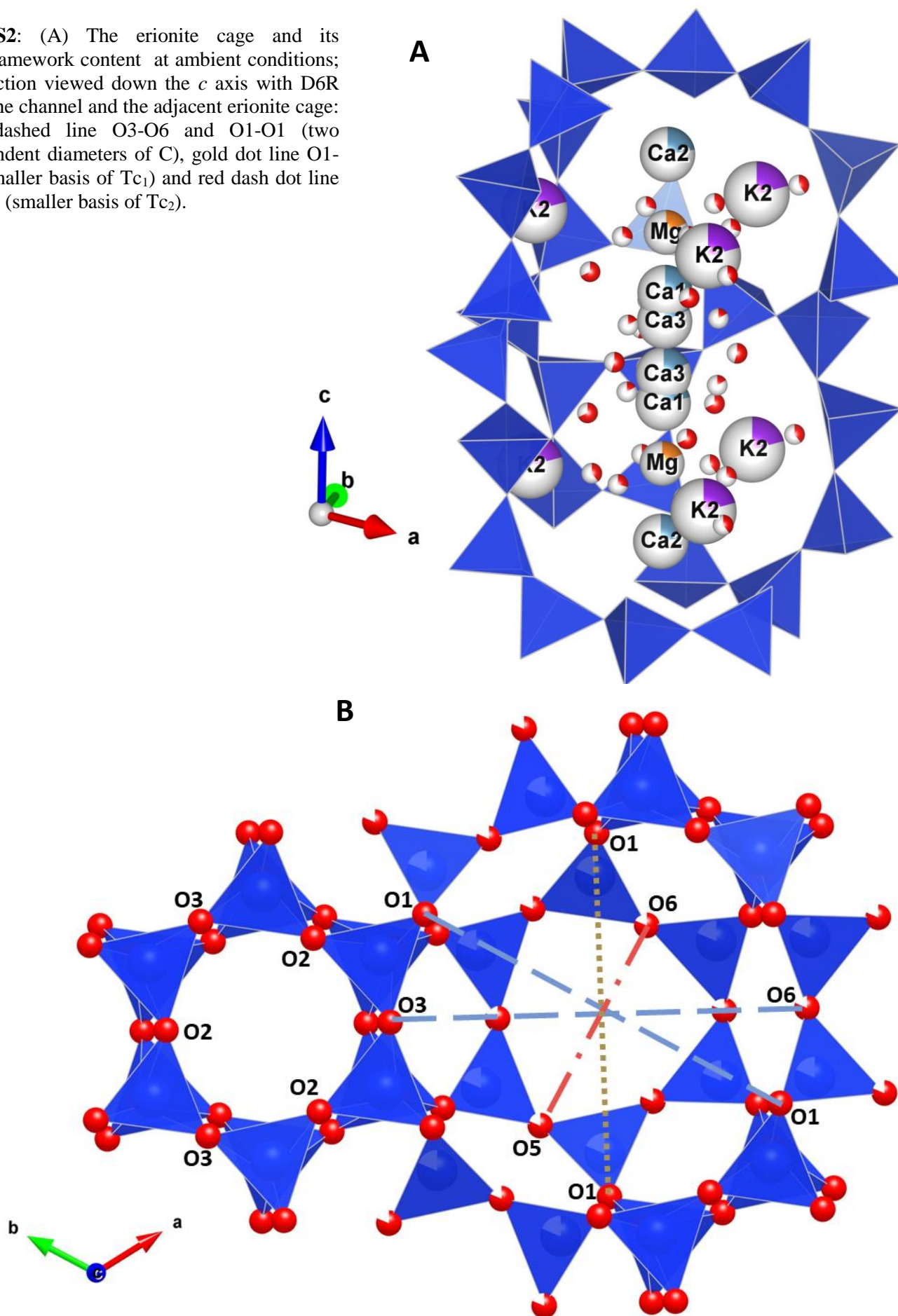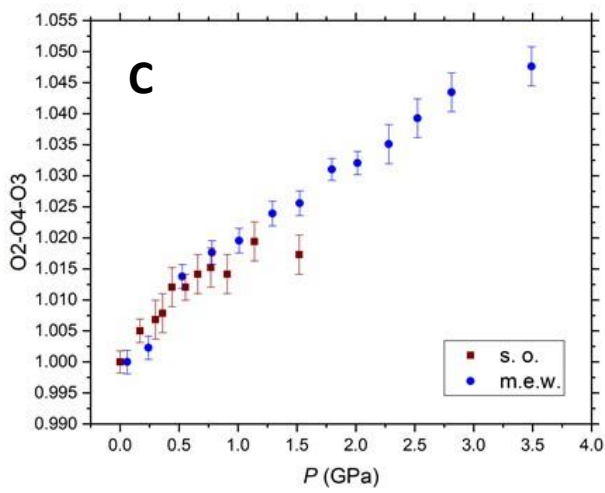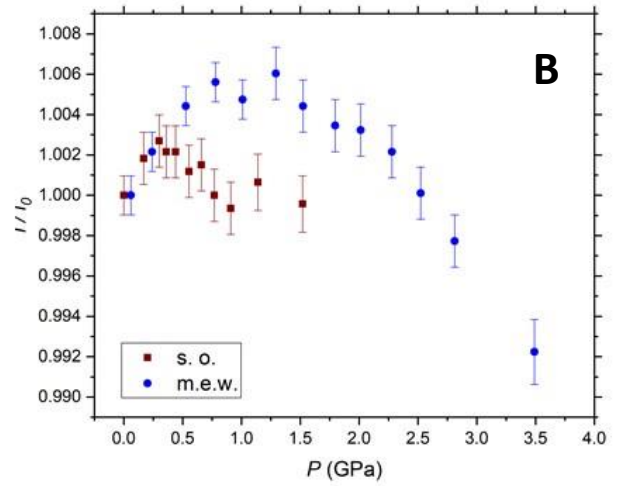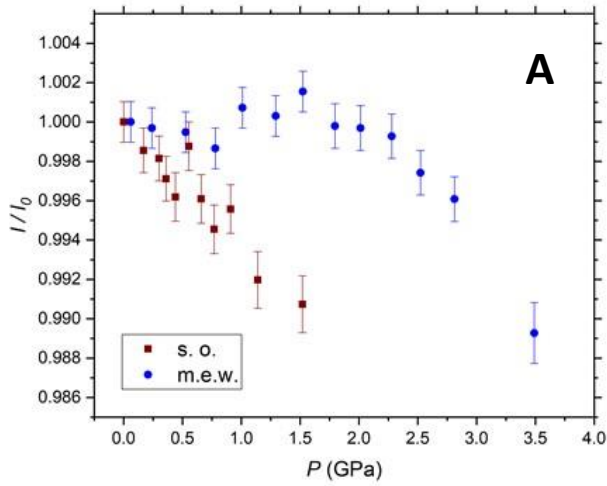
Fig. S3: *P*-induced evolution in silicone oil (red squares) and methanol:ethanol:water (16:3:1) (blue circles), of normalized (to ambient-*P* values): (A) O3-O6 independent diameter of the erionite-cage (see Fig. S12); (B) O1-O1 independent diameter of the erionite-cage (see Fig. S2b); (C) O2-O4-O3 opening angle of the D6R (see Fig. 1b)

625

626

627

628

629

630

631

632

633

634

635

636

637

638

639
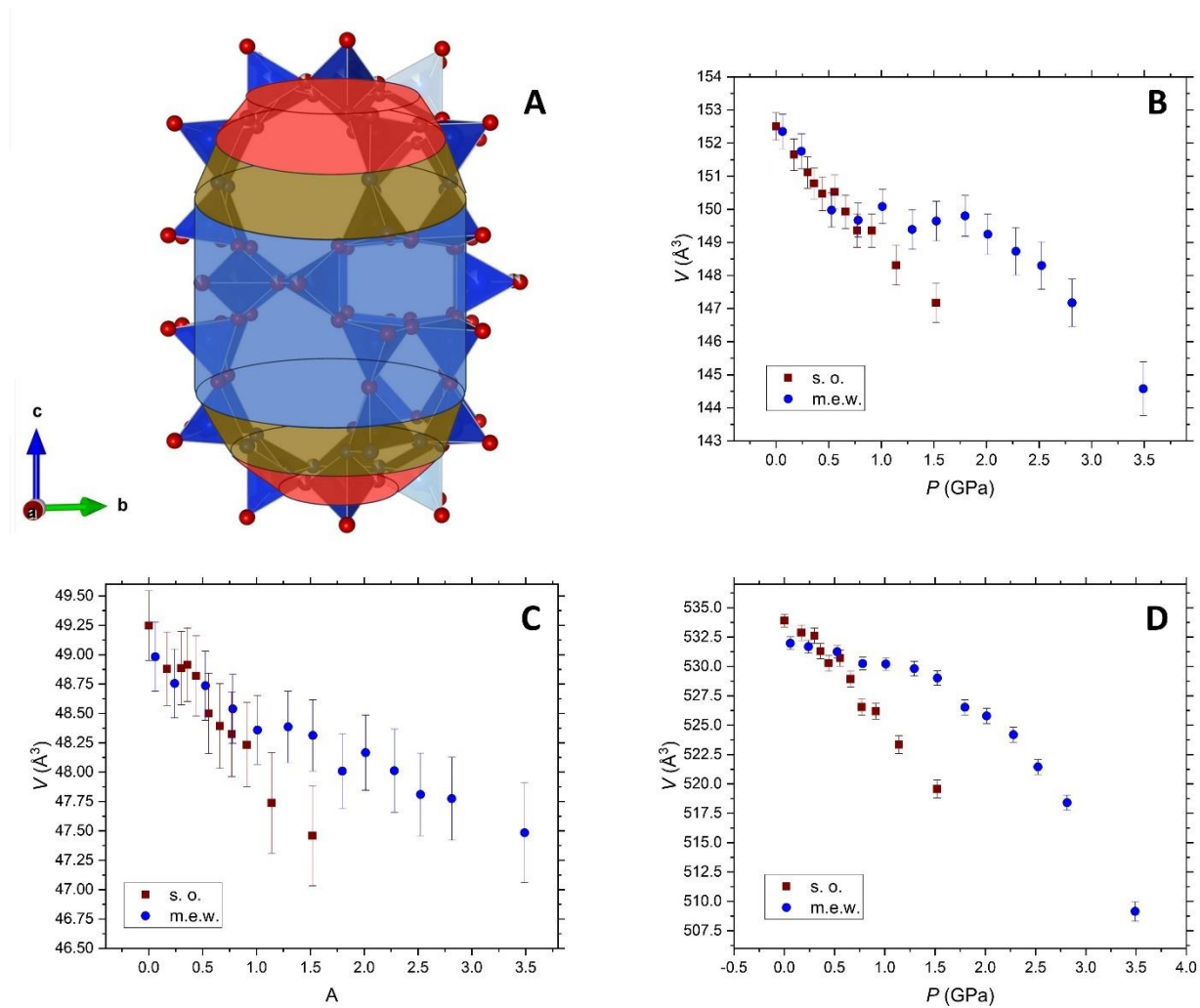
Fig. S4: (A) solid shape used to model the *P*-induced evolution of the volume of the erionite cage: blue cylinder (C), gold truncated cones (Tc1) and red truncated cones (Tc2); *P*-induced evolution in silicone oil (red squares) and methanol:ethanol:water (16:3:1) (blue circles), of the solids used to model the *eri*-cage volume: (B) Tc1; (C) Tc2; (D) C, cylinder.